



Multiscale Modeling of Anchor Pullout in Sand

Weijian Liang, Ph.D.¹; Jidong Zhao, Ph.D.²; Huanran Wu, Ph.D.³; and Kenichi Soga, Ph.D., F.ASCE⁴

Abstract: Pullout of plate anchors from granular sands is investigated using a novel computational multiscale approach. We employ the material point method (MPM) to solve a large deformation boundary value problem and adopt the discrete element method (DEM) to derive the history-dependent material responses required for each material point of the MPM domain. The continuum-discrete hierarchical coupling between MPM and DEM not only helps to bypass the assumption of complicated phenomenological constitutive models for sand, but also facilitates the handling of large displacement movement of the anchor and its ensuing complicated interactions with surrounding soil. This multiscale method is used to simulate the pullout of both horizontally and vertically placed plate anchors in sand by a large displacement, and to examine the roles of key factors, including the relative density of sand and the embedment depth, on the bearing capacity and pullout behavior. For a horizontally placed plate anchor, a truncated cone shape of soil body is mobilized upward at shallow embedment depth, whereas at greater depths, the surrounding soil may flow from the top to the bottom of the anchor, forming an interesting circulating circular shape. For a vertically placed plate anchor, the failure pattern of soil evolves gradually from a general shear failure mode to a local rotational failure mode when the embedment depth is increased. The study also provides cross-scale insight for the macroscopic observation on anchor pullout and comparisons with past studies. DOI: [10.1061/\(ASCE\)GT.1943-5606.0002599](https://doi.org/10.1061/(ASCE)GT.1943-5606.0002599). © 2021 American Society of Civil Engineers.

Author keywords: Anchor; Large deformation; Multiscale modeling; Material point method.

Introduction

Anchors offer popular and efficient solutions for both onshore and offshore geotechnical engineering to provide resistance against uplift or lateral loading. For example, mooring systems using anchors have been widely used for buoyant platforms, transmission towers and sheet pile walls (Randolph and Gourvenec 2017; Das and Shukla 2013). The design of anchors in on/offshore soil foundation is generally considered challenging due to the wide range of complexities involved, including complex loading conditions and load combinations (e.g., wind, wave, and others) and complicated anchor-soil (and water, for offshore engineering) interactions. The bearing capacity of supporting soil resisting the pullout of anchors has been a primary design index.

Over the past several decades, there have been numerous studies on the subject using either experimental or numerical tools, leading to considerable advances towards the understanding of anchors for anchor design. Both small-scale laboratory tests (Balla 1961; Vesić and Jones 1971; Murray and Geddes 1987; Ilamparuthi et al. 2002; Liu et al. 2012, 2013; Han et al. 2016; Choudhary and Dash 2017; Cheuk et al. 2008) and centrifuge physical modeling (Dickin and Leung 1985; Dickin 1988; Dickin and Laman 2007) have been attempted. Numerical modeling of anchors has been predominantly

based on the limit equilibrium method, limit analysis, and other continuum methods. For example, the limit equilibrium method (Biazee et al. 1965; Vesić and Jones 1971; White et al. 2008) has prevailed in practical design where the bearing capacity of an anchor is normally obtained with presumed failure surfaces under static equilibrium conditions. Limit analysis (Merifield and Sloan 2006; Smith 2012) yields more rigorous results of the limit pullout loads for anchors, based on assumptions of statically or dynamically admissible fields. However, it can only estimate the collapse load according to the initial geometry, and cannot offer the load-displacement response of the anchor or account for progressive failure with significant geometric changes during the anchor pullout process. Continuum methods, such as those based on Finite Element Method (FEM) (Rowe and Davis 1982; Yang and Yu 2010; Merifield and Sloan 2006; Yimsiri et al. 2004; Roy et al. 2018a, b) and Material Point Method (MPM) (Coetzee et al. 2005; Ceccato et al. 2020), have also been adopted to model the anchor pullout process.

Despite the great successes of the various methods in modeling anchor problems, they are not without limitations. For example, conventional Lagrangian FEM may encounter difficulties in modeling large displacements or rotations of soils commonly associated with anchor pullout, due primarily to mesh distortion and other numerical issues. The majority of existing FEM simulations on anchor pullouts are therefore terminated at a small displacement regime. Though numerical techniques such as remeshing or adaptive meshing (Hu and Randolph 1998; Yu et al. 2008) can be used to alleviate this issue, they commonly demand excessive computational effort and may incur further errors. Indeed, when mapping the stress, strain, and other state variables from the old mesh to the new one, inappropriate interpolation or less rigorous implementation could lead to nonequilibrium, noncompatibility of the whole domain and thereby inaccurate predictions (Hu and Randolph 1998; Tian et al. 2015). Frequently, these continuum numerical methods require assuming a constitutive model to describe the soil behavior at each material point (e.g., integration point in FEM). Indeed soil behavior is known to be highly nonlinear, loading history dependent, and extremely challenging to model (Yang and Yu 2010; Roy et al. 2016),

¹Postdoctoral Research Fellow, Dept. of Civil and Environmental Engineering, Hong Kong Univ. of Science and Technology, Hong Kong. Email: wliangab@connect.ust.hk

²Professor, Dept. of Civil and Environmental Engineering, Hong Kong Univ. of Science and Technology, Hong Kong (corresponding author). ORCID: <https://orcid.org/0000-0002-6344-638X>. Email: jzhao@ust.hk

³Assistant Professor, School of Civil Engineering, Chongqing Univ., Chongqing 400045, China. Email: hwucqu@163.com

⁴Chancellor's Professor, Dept. of Civil and Environmental Engineering, Univ. of California, Berkeley, CA 94720. Email: soga@berkeley.edu

Note. This manuscript was submitted on May 6, 2020; approved on April 26, 2021; published online on July 6, 2021. Discussion period open until December 6, 2021; separate discussions must be submitted for individual papers. This paper is part of the *Journal of Geotechnical and Geoenvironmental Engineering*, © ASCE, ISSN 1090-0241.

and it becomes excessively so for anchor pullout problems where soil-anchor interactions and large deformations may play a dominant role. However, oversimplified constitutive models, such as the Mohr-Coulomb model, remain dominant in practical design.

Meanwhile, the discrete element method (DEM) has become a popular numerical tool in recent years for investigating soil behaviors through all deformation regimes and under variable loading conditions, without having to resort to complex phenomenological assumptions. Based on relatively simple granular physics at the individual particle level, DEM can faithfully reproduce the complex collective mechanical behavior of an assembly of granular media, such as strain softening, fabric anisotropy and liquefaction (Wei et al. 2020; O'Sullivan et al. 2008; Zhao et al. 2018). Despite DEM's unprecedented capability in modeling small-size granular samples, it remains unfeasible to offer meaningful predictions for practical engineering problems. Its predictive capabilities are largely limited by the number of particles it models, the available computational resources, and the extent to which natural morphology and surface characteristics of grains can be reproduced.

Herein, a newly developed multiscale approach (Liang and Zhao 2017, 2019) based on coupled MPM and DEM is employed to systematically investigate the behavior of anchors and adjacent soil during the pullout process. This multiscale approach invokes MPM to tackle large deformation problems on the macroscale, and employs DEM to reproduce the soil response from the particle scale. It helps bypass the need for phenomenological constitutive models that are indispensable for conventional continuum modeling, and generates realistic soil responses under general loading conditions, based on a discrete consideration of soil particles. A hierarchical coupling structure between MPM and DEM also makes it feasible to probe fundamental microstructural mechanisms underpinning interesting macroscopic phenomena or observations, providing quantitative cross-scale correlation and reliable physical interpretations. This multiscale modeling approach will be employed to model the pullout from granular soils of horizontally and vertically placed plate anchors. We thoroughly examine the influences of three key factors, including the relative density of sand, the embedment ratio, and the anchor orientation, on all aspects of the behavior of anchors (e.g., bearing capacity, deformation patterns, and failure mechanisms). Mesoscopic data and analyses originated from the particle scale will be provided in lieu of various failure patterns observed in our simulations.

Coupled MPM-DEM Multiscale Approach

The multiscale approach is based on hierarchical coupling of a MPM solver [NairnMPM (Nairn 2016)] with a DEM solver [YADE (Smilauer et al. 2015)] to solve a large deformation problem. Representative Volume Elements (RVEs), consisting of granular particles, are first generated in the DEM solver and then assigned to the material points in the MPM domain. Depending on the specific problem, the assigned RVEs can be identical or variable, leading to a homogeneous or inhomogeneous continuum domain. During each coupling cycle, MPM is first invoked to produce the deformation information (typically, the incremental displacement gradient) of each material point. The deformation information is then transferred to the assigned RVE at the material point, serving as the boundary condition for the DEM solver as a mesoscale boundary value problem. Cauchy stress is homogenized over the deformed packing and is then sent back to the MPM solver to advance its subsequent computation, e.g., calculating the nodal force and updating the material points positions. After each loading step, the deformed RVE is recorded as the initial state for the subsequent loading step.

In doing so, the multiscale modeling keeps a memory of the past loading history of each material point over the whole domain, and faithfully and flexibly reproduces complex soil behavior under various loading conditions. The following only provides a brief outline of solvers in separated scales for the sake of completeness; readers can refer to Liang and Zhao (2019) for the rigorous derivation and complete formulation of the coupled MPM-DEM multiscale framework.

Macroscale Solver: MPM

The movement and deformation of any arbitrary material in a continuum domain discretized by MPM is governed by the conservation of mass and momentum as well as a constitutive law:

$$\frac{D\rho}{Dt} = 0 \quad (1)$$

$$\rho \frac{Dv}{Dt} = \nabla \cdot \sigma + \rho g \quad (2)$$

$$\sigma = f(F) \quad (3)$$

where σ = Cauchy stress tensor; and F = deformation gradient.

In MPM, the material is represented by a set of points which carry mass, momentum, and deformation information. Mass conservation and momentum equations are formulated according to a Lagrangian description. To simplify the calculation of the spatial derivatives of the stress tensor $\nabla \cdot \sigma$ and the deformation gradient F , MPM adopts a regular background Eulerian mesh as a scratch pad, which enables the interpolation of information at a grid node by its surrounding material points and vice versa. This also facilitates the integration of the following weak form of momentum equation on the node:

$$\dot{p}_I = f_I^{int} + f_I^{ext} \quad (4)$$

with

$$\dot{p}_I = \sum_p \dot{p}_p S_{Ip} \quad (5)$$

$$f_I^{int} = - \sum_p \sigma_p \cdot \nabla S_{Ip} V_p \quad (6)$$

$$f_I^{ext} = \sum_p m_p b S_{Ip} + \int_{\partial\Omega} N_I \tau dS \quad (7)$$

where \dot{p}_I = material time derivative of nodal momentum; f_I^{int} and f_I^{ext} = internal and external forces, respectively, acting on the node; \dot{p}_p = material time derivative of material point momentum; σ_p = Cauchy stress tensor at the material point; V_p and m_p = volume and mass of the material point; τ = boundary traction; N_I = shape function; and S_{Ip} and ∇S_{Ip} = weighting function and its gradient, respectively (c.f. Bardenhagen and Kober 2004; Liang and Zhao 2019). After the momentum equation is solved, the new information can be interpolated from grid nodes back to material points to update the state of material points.

Conventional MPM modeling requires a constitutive model to describe the response for each of the material points. In the coupled MPM-DEM multiscale framework, the mechanical material response is produced by a DEM solution of the RVE attached to each material point, therefore bypassing the need for assumed phenomenological constitutive models.

Mesoscale Solver: DEM

DEM is used to provide a solution to each RVE attached to a material point in the MPM subjected to each incremental deformation/displacement boundary condition. In DEM, the contact forces (including normal contact force f_n^c , tangential/shear contact force f_t^c , and rolling resistance M_r^c) between two contacting particles are calculated as

$$f_n^c = -k_n^c \delta n \quad (8)$$

$$f_t^c = -\min(k_t^c u_t, f_n^c \tan \varphi) t \quad (9)$$

$$M_r^c = -\min(k_r^c \theta_r, f_n^c r_{\min} \eta) \theta_r / |\theta_r| \quad (10)$$

where k_n^c , k_t^c , and k_r^c = normal contact stiffness, tangential (shear) contact stiffness, and rolling stiffness, respectively; δ = contact overlap; u_t = relative shear displacement; θ_r = accumulated relative rotation angle; φ = inter-particle friction angle; r_{\min} = radius of the smaller particle; and n and t = unit normal vector and unit tangential vector of the contact, respectively. In the DEM community, two contact models, namely, linear force-displacement and Hertz-Mindlin (Mindlin and Deresiewicz 1953; Yimsiri and Soga 2000; Zhao et al. 2018), have been commonly used to determine contact stiffnesses. The former considers contact stiffnesses as constants, whereas the nonlinear Hertz-Mindlin model assumes these two parameters vary with the contact overlap. Following (Liang and Zhao 2019), we herein employ the linear force-displacement contact model to calculate the contact force, because of its simplicity. In the linear force-displacement model, the contact stiffnesses (k_n^c , k_t^c and k_r^c) are determined by the following:

$$k_n^c = Er^* \quad (11)$$

$$k_t^c = \nu Er^* \quad (12)$$

$$k_r^c = k_t^c r_i r_j \beta \quad (13)$$

where E = Young's modulus; $r^* = 2r_i r_j / (r_i + r_j)$ = harmonic mean of radii of the contacting particles; $\nu = k_t^c / k_n^c$ = stiffness ratio; and β is a dimensionless coefficient.

In our MPM-DEM coupling, the only essential information needing to be retrieved from the DEM solver is the Cauchy stress tensor σ , which can be obtained by homogenizing over the deformed RVE according to the Love-Weber formula (Christoffersen et al. 1981; Nicot et al. 2013):

$$\sigma = \frac{1}{V} \sum_{N_c} d \otimes f^c \quad (14)$$

where \otimes denotes the dyadic product; V = volume of RVE; N_c = number of contact inside RVE; d = branch vector joining centers of contacting particles; and f^c = contact force.

Meanwhile, it is instructive to extract the fabric anisotropy (Satake 1982; Oda 1982) for helping the interpretation of the macroscopic observations:

$$\phi = \frac{1}{N_c} \sum_{N_c} n \otimes n \quad (15)$$

$$\mathbf{F}_a = 4 \left(\phi - \frac{1}{2} I \right) \quad (16)$$

$$\mathbf{F}_a = \sqrt{\frac{1}{2} \mathbf{F}_a : \mathbf{F}_a} \quad (17)$$

where $:$ = second-order tensor contraction; ϕ = fabric tensor (contact normal based); \mathbf{F}_a = deviatoric fabric tensor; and F_a is a scalar value used to measure anisotropy intensity.

Simulation of Plate Anchor Pullout

Model Setup

The model setup for plate anchors in sand, including horizontally placed anchor and vertically placed anchor, are shown in Fig. 1. As the focus of the study is the behavior of a strip plate anchor, all simulations were conducted under the assumption of plane strain condition, which lends great convenience and saves computational costs. For cases of horizontally placed plate anchors, only half of the domain was modeled, because of its symmetric nature. The anchor was considered perfectly rigid with rough surfaces. The soil domain was discretized in MPM by Eulerian elements, with an element size of 0.1 m and a particle-per-cell (PPC) number of 1. The total number of material points simulated ranges from 8,000 to 22,400, depending on the geometry of the soil domain (e.g., deeply embedded anchor cases need a deep soil domain). Note that, as with other conventional continuum methods, MPM may also suffer from mesh dependency in simulating post-peak behavior (Liang and Zhao 2019). A mesh-dependency study was performed in selecting the mesh size, and the result is presented in the Appendix. The RVEs to be assigned to the material points were first isotropically compressed (assuming $K_0 = 1$) in the DEM to different stress states, to reproduce the in-situ stress field changing with depth, i.e., $p_c = \rho h g$, where g = gravity and h = depth of the material point.

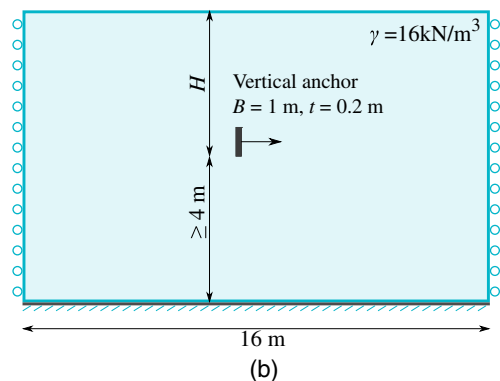
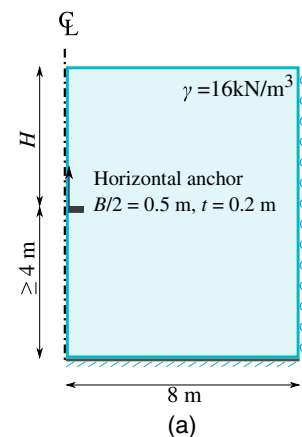


Fig. 1. Model setup for anchor in sand: (a) horizontally placed plate anchor; and (b) vertically placed plate anchor.

This prestressing process helps shorten the computational time needed for the system to reach equilibrium and avoids excessive change anchor position relative to the soil. For both horizontally and vertically placed plate anchors, the displacement for the anchor is denoted by d , and its maximum value is set to $d_{\max} = 0.4B$.

RVE Calibration

In this study, the DEM packings RVEs were generated based on the microscopic parameters listed in Table 1, following our previous study (Liang and Zhao 2019). The preparation of RVEs comprises two stages, namely, a consolidation stage and a rebalance stage. By changing the interparticle friction during the consolidation stage, one can generate RVEs with different relative densities (and porosities and dilation angles in terms of conventional models). In the present study, two RVEs with varied porosities were generated, representing dense (2D porosity: $n \approx 0.16$) and loose ($n \approx 0.20$) sand, respectively.

A series of biaxial compression tests were further conducted on the generated RVE packings under various confining pressures (i.e., 32, 64, and 128 kPa) by pure DEM simulations to obtain macroscopic frictional angles of the RVEs. The estimation of macroscopic parameters enables us to compare our multiscale predictions with the classic solutions reported in the literature. According to the calibration results shown in Fig. 2, the macroscopic friction angle φ' for the dense sand and the loose sand are estimated as 30.2° and 20.9° , respectively.

Table 1. Microscopic parameters for RVE generation

Parameter	Symbol	Value
Particle number	N	400
Radius	r (mm)	3–7
Density	ρ (kg/m ³)	2,650
Young's modulus	E (MPa)	800
Stiffness ratio	ν	0.5
Inter-particle friction angle	φ (°)	23
Rolling stiffness coefficient	β	1.0
Rolling resistance coefficient	η	0.05
Damping	α	0.1

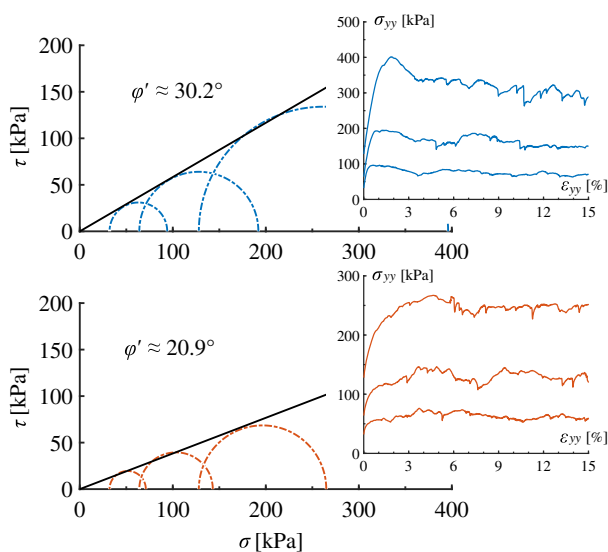


Fig. 2. Determination of macroscopic peak friction angle of RVEs; the responses of RVEs are from biaxial tests with confining pressures of 32, 64, and 128 kPa.

Notably, the friction angles determined by DEM for the generated RVEs as shown above are relatively lower as compared to real sand, such as Toyoura sand. The use of spherical particles in the RVEs may account for the difference. Indeed, the non-spherical shape of real sand grains may lead to substantial interlocking and enhanced internal friction greater than the idealized case considered in the study. Although further consideration of rolling resistance in the DEM may reduce the difference (Zhao and Guo 2014), it cannot reproduce the many complicated interlocking behaviors widely observed in natural granular materials (Cui et al. 2007). More realistic modeling of granular media can be achieved by incorporating particle morphology into the DEM simulations, e.g., LS-DEM (Kawamoto et al. 2018) and poly-superellipsoid particles (Zhao and Zhao 2019), which will be pursued in future studies.

Bearing Capacity of Anchor Pullout

Load-Displacement Responses

The typical load-displacement responses of a plate anchor pulled out from sand are plotted in Fig. 3. We first examine the cases of horizontally placed plate anchors. As shown in Fig. 3(a), the resistance acting on a horizontally placed plate anchor evolves similarly for different burial depths (denoted by embedment ratio H/B) when it is pulled out vertically (denoted by normalized displacement d/B). In dense sand, the resistance imposed on the anchor

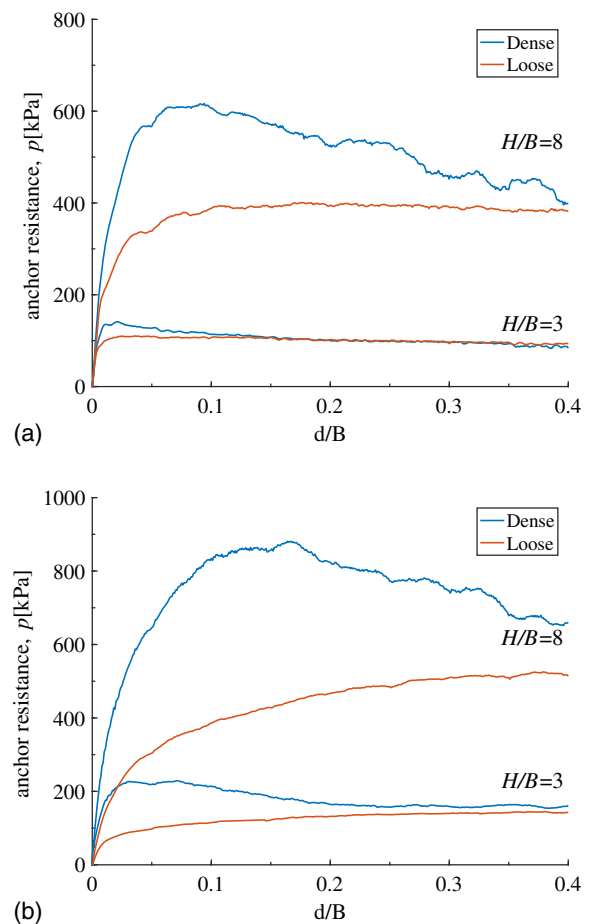


Fig. 3. Load-displacement responses for pullout of (a) horizontally placed plate anchor; and (b) vertically placed plate anchor, both from sand.

will develop a rather brief initial elastic stage followed by a non-linear increase before reaching a peak, then show a steady decrease associated with a softening stage of the curve. The peak resistance occurs at a smaller displacement $d/B = 0.02$ for the shallow embedment ($H/B = 3$) than the deep one ($d/B = 0.08$ for $H/B = 8$). Such strain-softening response may not be well captured merely by simplified constitutive models, i.e., the standard Mohr-Coulomb model (Roy et al. 2016, 2018a; Coetzee et al. 2005; Ceccato et al. 2020). At the end of a cutoff pulling displacement ($d/B = 0.4$), the drop rate of resistance does not seem to change appreciably, indicating a steady (if not accelerating) failure of the load-bearing soil during the anchor pullout. To pull out a horizontally placed plate anchor from loose sand, the resistance increases gradually with pullout displacement and reaches a steady value when the mobilized displacement is significant; deeper embedment generally leads to a higher steady resistance. However, a larger displacement is needed for a deeply embedded anchor to reach peak resistance, compared to a shallow anchor. Interestingly, for a given embedment depth, especially for the shallow case, the anchor resistances converge to a “critical state like” value for both dense and loose cases (Schofield and Wroth 1968). Possible correlation between this convergence of anchor bearing resistance and sand behavior within the localized shear zones will be detailed in subsequent mesoscale analyses.

The load displacement responses for a vertically placed anchor subjected to horizontal pulling, as shown in Fig. 3(b), share certain similarities with horizontally placed anchor cases, but with distinctive differences. Compared to its horizontally placed counterpart, a vertically placed anchor reaches peak resistance at a slower pace in dense sand. In loose sand, the resistance for a vertically placed plate anchor shows a steadily increasing trend throughout the pulling process, in contrast to an almost constant value for the horizontally placed anchor. This discrepancy may arise from the fact that different soil masses would be involved and densified when the pulling direction varies. For example, pulling out a vertically placed plate anchor may have to mobilize and densify an increasing volume of soil compared to the horizontally placed plate anchor, as the latter moves toward the free ground surface. The above finding agrees well with the observations in Rowe and Davis (1982) and Choudhary and Dash (2017).

Break-Out Factor

A dimensionless break-out factor N_γ has commonly been adopted to measure the bearing capacity of anchors in sand (Rowe and Davis 1982; Merifield and Sloan 2006):

$$N_\gamma = q_u / \gamma H \quad (18)$$

where q_u = ultimate capacity of anchor, being correlated with the ultimate load Q_u via $q_u = Q_u/B$; γ = unit weight of the soil; and H = embedment depth of the anchor. Specifically, the ultimate load of anchor Q_u is taken at a point where the slope of the load displacement curve first reaches either 0, or a steady and minimum value, following the definition in Vesić (1973).

For a horizontally placed plate anchor subjected to vertical pullout, Meyerhof and Adams (1968) indicated that its breakout factor in cohesionless soil can be calculated as follows:

$$N_\gamma = \frac{H}{B} K_u \tan \varphi' + 1 \quad H \leq H_{cr} \quad (19)$$

$$N_\gamma = \left(2 - \frac{H_{cr}}{H}\right) \left(\frac{H_{cr}}{B}\right) K_u \tan \varphi' + 1 \quad H > H_{cr} \quad (20)$$

where K_u = nominal uplift coefficient of earth pressure, and is suggested to be equal to 0.95 for a strip anchor; and H_{cr} = the vertical

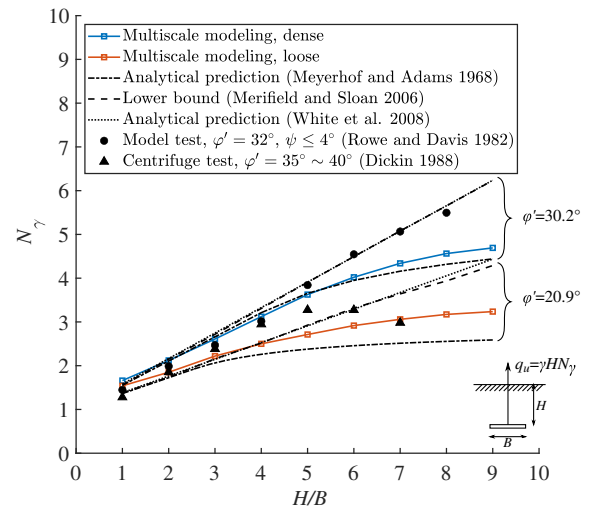


Fig. 4. Variation of break-out factor with burial depth for pullout of a horizontally placed plate anchor in sand.

extent of the failure surface, and can be approximated from Table 1 in Meyerhof and Adams (1968). Meanwhile, H_{cr} has also been termed as “critical depth” by Das and Shukla (2013), which indicates the transition from shallow to deep anchor.

Fig. 4 shows the variation of break-out factor N_γ of a horizontally placed plate anchor with embedment ratio H/B predicted by our multiscale simulations, in comparison with results from the literature (Meyerhof and Adams 1968; Merifield and Sloan 2006; White et al. 2008; Rowe and Davis 1982; Dickin 1988). The break-out factor of plate anchor in dense sand increases almost linearly at shallow embedment depths, whereas its increase rate drops when the embedment ratio is greater than 5 ($H/B > 5$). The bearing capacity for an anchor in loose sand shares a similar trend, except that its decrease in slope takes place at a smaller embedment ratio (e.g., $H/B = 4$). Our multiscale predictions agree remarkably well with the analytical solutions provided by Meyerhof and Adams (1968) over 50 years ago, especially for the dense sand case. Meanwhile, moderate discrepancies can be observed between our predictions and the limit analysis results from (Merifield and Sloan 2006), especially at a larger embedment ratio. The possible cause of this difference is twofold. First, the limit analysis adopts a perfect plasticity model where the post-peak softening behavior of soil is regarded as irrelevant. Since most failures in soil are progressive, it may occur that part of a soil body has already failed and entered a softening regime while the rest remains in a hardening regime. Moreover, a lower bound limit analysis is typically conducted based on the initial geometry of the soil without accounting for the geometry change during the anchor pullout process. There is a mild discrepancy between the current result and the limit equilibrium solution (White et al. 2008), which assumes an inverted trapezoidal shape mobilization region and peak soil resistance along the slip surfaces. This discrepancy could be attributed to the fact that the mobilization region in the present study is not an exact inverted trapezoidal shape, especially at large embedment ratios. Fig. 4 also shows that the MPM-DEM results lie between the model test result by Rowe and Davis (1982) and the centrifuge result by Dickin (1988).

To examine the peak resistance of anchors in ultradeep burial depths, two additional tests with $H/B = 20$ and $H/B = 50$ were conducted. We adopted the same geometry for case $H/B = 9$ and apply a surcharge ($q_s = 11B\gamma$ for $H/B = 20$ and $q_s = 41B\gamma$ for

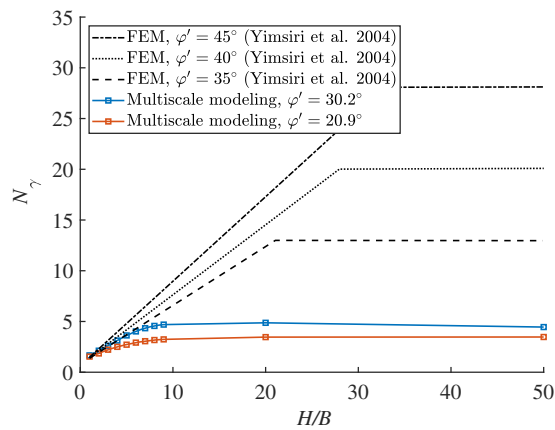


Fig. 5. Breakout factor for ultra-deep horizontally placed plate anchor.

$H/B = 50$) on the ground surface to achieve a high stress state. In doing so, considerable computational costs were avoided. The multiscale result is plotted in Fig. 5 in comparison with the design chart value from (Yimsiri et al. 2004). Note that the design chart has been constructed from FEM analysis of small diameter pipe in medium to dense sands, based on the Mohr-Coulomb perfectly plastic soil model and the NorSand critical state model. Therefore the comparison should be taken as more qualitative rather than quantitative. In particular, the design chart has adopted soil parameters for medium to dense sand with frictional angles between 35° and 45° , suggesting critical breakout factors ranged from 13 to 28. The present MPM-DEM modeling has adopted a round spheres with simple contacts model and hence much smaller frictional angles ($\varphi' = 30.2^\circ$ and 20.9° for the two cases considered), leading to critical breakout factors close to 4.8 and 3.5, respectively.

For vertically placed plate anchors, the breakout factor is found to increase with the embedment ratio, as shown in Fig. 6. The increase is almost linear at shallow embedment depths. However, our predictions show that this increase of breakout factor with embedment ratio rapidly curves down to reach a plateau steady curve when the embedment ratio is deeper (from $H/B = 4$ for dense sand and $H/B = 3$ for loose sand). The steady value of the breakout factor is around 6.4 for dense sand and 4.1 for loose sand. Because of the larger friction angle, the experimental result by Dickin and Leung (1985) yields a higher breakout factor. Again, the limit analysis results reported by Merifield and Sloan (2006) show significant overestimations of the bearing capacity as compared to ours. Comparatively, the analytical solution of Meyerhof (1973) provides a good prediction for intermediate embedment depth (e.g., $4 < H/B < 7$). Intriguingly, our multiscale modeling predictions match almost perfectly with the semianalytical solutions provided by Biarez et al. (1965), for both dense and loose sand cases over all embedment ratio ranges. In their analyses, Biarez et al. (1965) assumed that the failure of a deep vertically placed plate anchor could be characterized by a local rotational mechanism where the soil adjacent to the moving anchor rotates around the upper edge of the anchor. Based on this mechanism and consideration of the equilibrium of torques for the soil cylinder, the breakout factor was derived as follows (Biarez et al. 1965):

$$N_\gamma = 4\pi(1 - B/H) \tan \varphi' \quad (21)$$

Although Eq. (21) was originally derived for deep strip anchors, it offers a satisfactory prediction for shallow vertically placed plate anchors, as depicted in Fig. 6. This may imply that the rotational failure mechanism may apply for both shallow and deep vertically

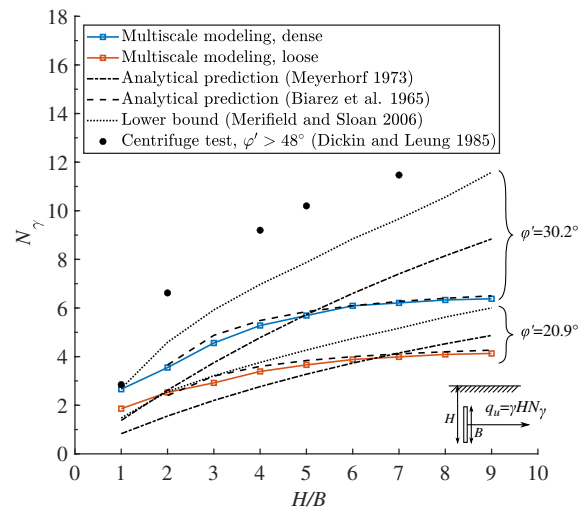


Fig. 6. Variation of breakout factor with burial depth for pullout of vertically placed plate anchor in sand.

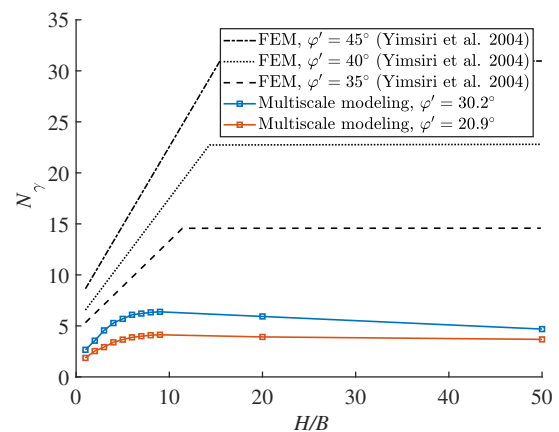


Fig. 7. Breakout factor for ultra-deep vertically placed plate anchor.

placed plate anchors. A verdict on this statement will be made in a subsequent section. Fig. 7 further presents a qualitative comparison of the breakout factor for vertically placed plate anchors at ultra-deep embedments between the design chart (Yimsiri et al. 2004) and the present multiscale predictions. In the lower friction angle case, both predictions by Yimsiri et al. (2004) and our multiscale breakout factor modeling show a rather consistent trend of steady increase with embedment depth at shallow depths, before reaching a steady constant value when $H/B \geq 9$. However, for the large frictional angle case, our multiscale prediction shows a minor drop in the breakout factor when the anchor becomes deeper; e.g., for dense sand N_γ decreases from 5.93 to 4.69 when H/B increases from 20 to 50, as compared to the constant prediction by Yimsiri et al. (2004). Further verification with similar friction angles, which necessarily requires the introduction of either grain shapes or rolling resistance and thus complicates the modeling, will be pursued in the future. It worth pointing out that the bearing capacity for an anchor is subject to an appreciable scale effect (Roy et al. 2018a; Dickin 1988), e.g., the dimensions of the anchor. Therefore, the general conclusion of this section, which was reached based on two-dimensional modeling of a 1 m wide anchor, should be interpreted with caution when extending to other conditions.

Deformation Patterns in Pullout of a Horizontally Placed Plate Anchor

Displacement Field

The displacement field in sand formed at the end of the pullout of a horizontally placed plate anchor is shown in Fig. 8. For a shallow anchor (e.g., $H/B = 2$), the soil immediately above the anchor is lifted vertically upwards and forms a heave on the ground surface. A clear cavity is formed underneath the anchor, with mild sideway soil body cave-ins. For shallow anchors, the relative density of the soil is found to have a minor effect on the deformation pattern, except that the horizontal extension of ground heave is slightly wider in the dense sand case (around $1.3B$ from the center) than for the loose sand case (around $1.1B$). With deeper burial depths, however, the effect of sand density becomes notable. Take the case of intermediate burial depth (e.g., $H/B = 5$) as an example: A conic shape of soil is mobilized upward to form a heave at the ground surface in the dense sand, which was also observed in the experimental tests by Liu et al. (2012). However, no appreciable surface heave is found as compared to the shallow one in Fig. 8(a), but its horizontal extension is much wider, amounting to $2.4B$ from the centerline. Distinguished nonuniform deformation inside the conic mobilization zone is also observed. Specifically, a triangular wedge appears immediately above the anchor wherein the soil is mobilized predominantly vertically as if it was part of the anchor, akin to the Rankine active zone in the classic footing problem (Terzaghi 1951). As for the case of loose sand with an embedment ratio of $H/B = 5$ [Fig. 8(d)], the mobilization zone shows approximately a bubble shape that is much smaller than the dense sand case and with a blurred boundary. Ground heaving is hardly observed, due apparently to the high compressibility of the loose sand. As the embedment becomes deeper, the cavity formed underneath the anchor also becomes confined and smaller for both dense and loose sand, which is probably attributed to the higher earth pressure at deeper embedment depths.

The soil deformation pattern for an even deeper anchor (e.g., $H/B = 8$) is entirely different from those mentioned previously. With further increases in embedment depth, the soil mass above the anchor is so heavy that the failure surface is prevented from reaching the ground surface, and thus the failure and movement of soil can only be confined within a local area in the vicinity of the anchor. In the case of dense sand [Fig. 8(e)], the aforementioned conic mobilization area is hardly recognizable. Instead, a distinct circle with a radius of $0.5B$ appears near the edge of the anchor. Within this circle, the soil above the anchor flows around its edge and fills the cavity created underneath. A similar flow-around mechanism is also observed in the loose sand [Fig. 8(f)], although its influence area extends further and does not follow a circular pattern. The flow-around mechanism in a deep horizontally placed plate anchor has also been reported in the literature (Wang et al. 2010; Chen et al. 2013).

Failure Patterns

Fig. 9 shows the contours of equivalent von Mises strain ε_{eq} ($= \sqrt{2/3} \varepsilon_q : \varepsilon_q$, where ε_q = deviatoric strain tensor) and rotation angle θ (retrieved from orthogonal rotation tensor $R = \begin{bmatrix} \cos \theta & -\sin \theta \\ \sin \theta & \cos \theta \end{bmatrix}$, with $R = F \cdot U^{-1}$, where F = deformation gradient and U = right stretch tensor) in sand at the end of the pullout of the horizontally placed plate anchor. At a shallow burial depth, the failure pattern features a major shear band, originating from the edge of the anchor, extending vertically upward and then curving sideways when it approaches the ground surface. The shear

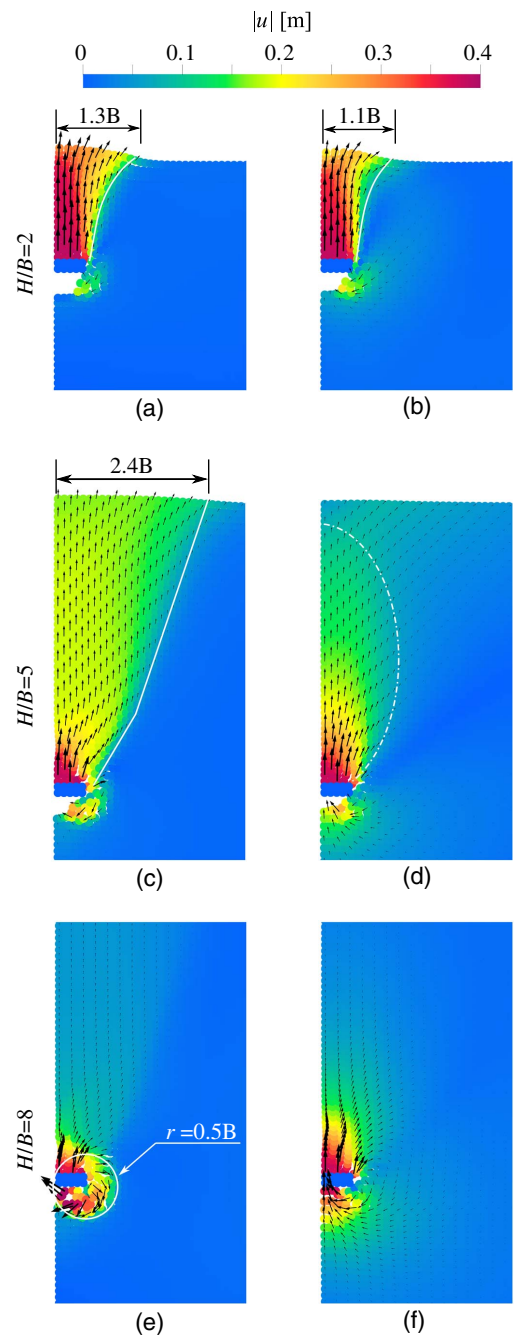


Fig. 8. Displacement field for horizontally placed plate anchors in sand at $d = 0.4B$: (a), (c), and (e), dense sand; and (b), (d), and (f), loose sand.

band angle to the horizontal plane varies from $\omega \approx 38^\circ$ in dense sand to $\omega \approx 46^\circ$ in loose sand. It is also easy to see that rotation occurs within the soil inside the shear band, and the cumulative rotation angle could amount to 50° .

When the burial depth is sufficiently deep (e.g., $H/B = 8$), the soil fails locally. As can be seen in Figs. 9(e and k), the shear failure zone for the case of dense sand is restricted within a circle around the anchor, wherein the soil inside rotates clockwise while that at the boundary rotates counterclockwise. The failure pattern of the loose sand is similar except that its shear intensity is relatively lower without apparent counterclockwise rotation, as compared to the dense sand case.

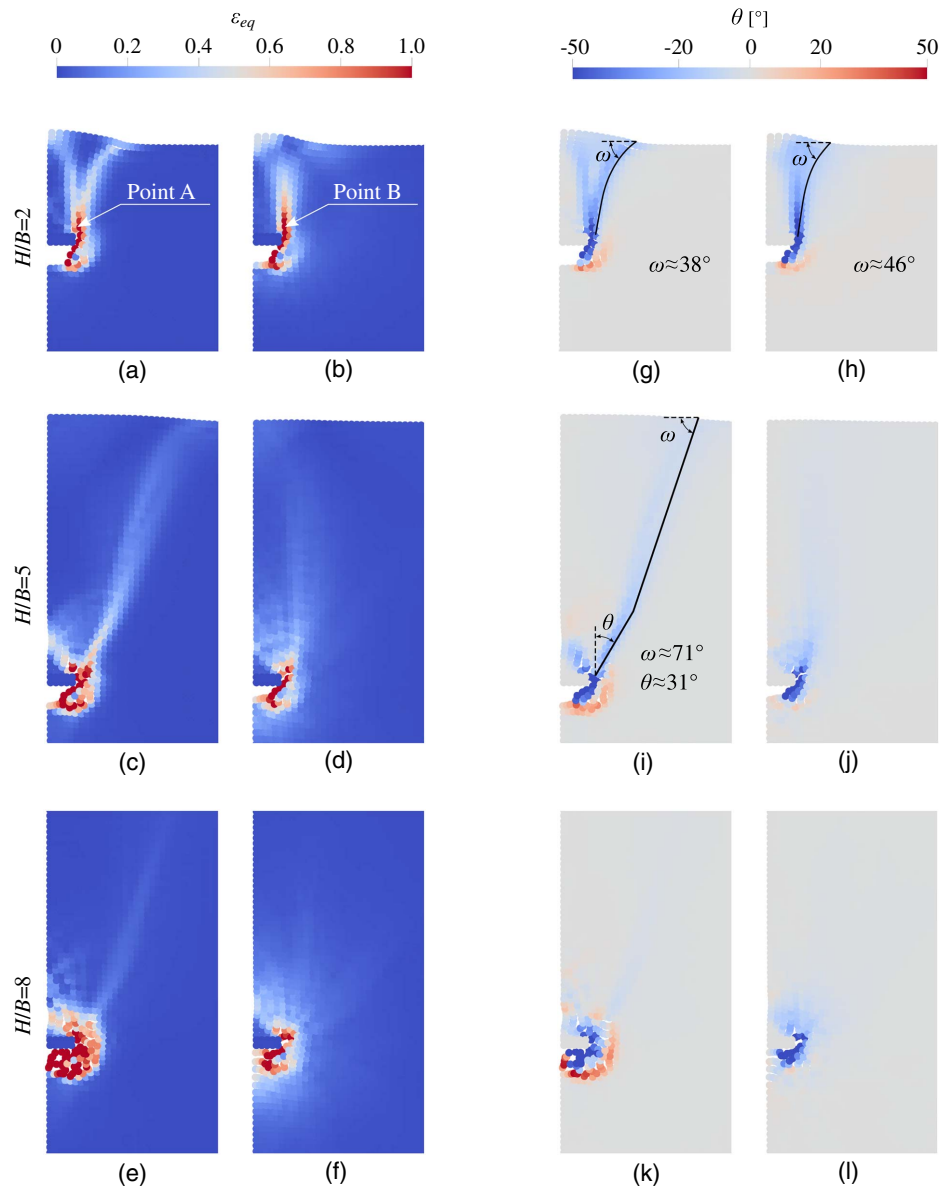


Fig. 9. Equivalent von Mises strain and rotation angle contour for horizontally placed plate anchors in sand at $d = 0.4B$: (a), (c), (e), (g), (i), and (k), dense sand; and (b), (d), (f), (h), (j), and (l), loose sand.

It is interesting to observe the transition of failure patterns in the case of intermediate embedment ratio $H/B = 5$, which are shown in Figs. 9(c, d, i, and j). For an anchor in dense sand, the failure pattern consists of two pronounced shear bands and a shear zone. The major shear band, having two segments, serves as the boundary of the mobilized area. It extends from the edge of the anchor with an inclined angle of $\theta = 31^\circ$, and penetrates the soil mass before intersecting with the ground surface at an angle of $\omega = 71^\circ$. Another shear band forms at the boundary of the triangular wedge and is much shorter than the major one. In addition to the two narrow shear bands, a shear zone is observed around the edge of the anchor, resembling that of the deep anchor. Similarly, the soil in the two shear bands and inside the shear zone rotates at a clockwise angle while that at the boundary of the shear zone rotates counterclockwise. As for the loose sand, only one shear band is captured, which originates at the edge of the anchor without reaching the ground surface. This failure pattern is relatively closer to that of the deep anchor than the shallow one.

Deformation Patterns in Pullout of a Vertically Placed Plate Anchor

Displacement Field

The displacement field in sand caused by the pullout of a vertically placed plate anchor is shown in Fig. 10. For a shallow anchor (e.g., $H/B = 2$), both dense sand and loose sand cases show a somewhat similar deformation pattern. When the anchor is pulled horizontally to the right, the soil ahead of the anchor is pushed to move forward and upward, forming an apparent heave at the ground surface, known as a Rankine passive failure (Terzaghi 1951). In this passive zone, the soil immediately in front of the anchor is moved forward along with the rough surface of the anchor, due to friction. Meanwhile, a Rankine active zone is formed behind the anchor, wherein the soil slides down along a slip surface to fill the gap left behind the anchor, forming a sink at the ground surface.

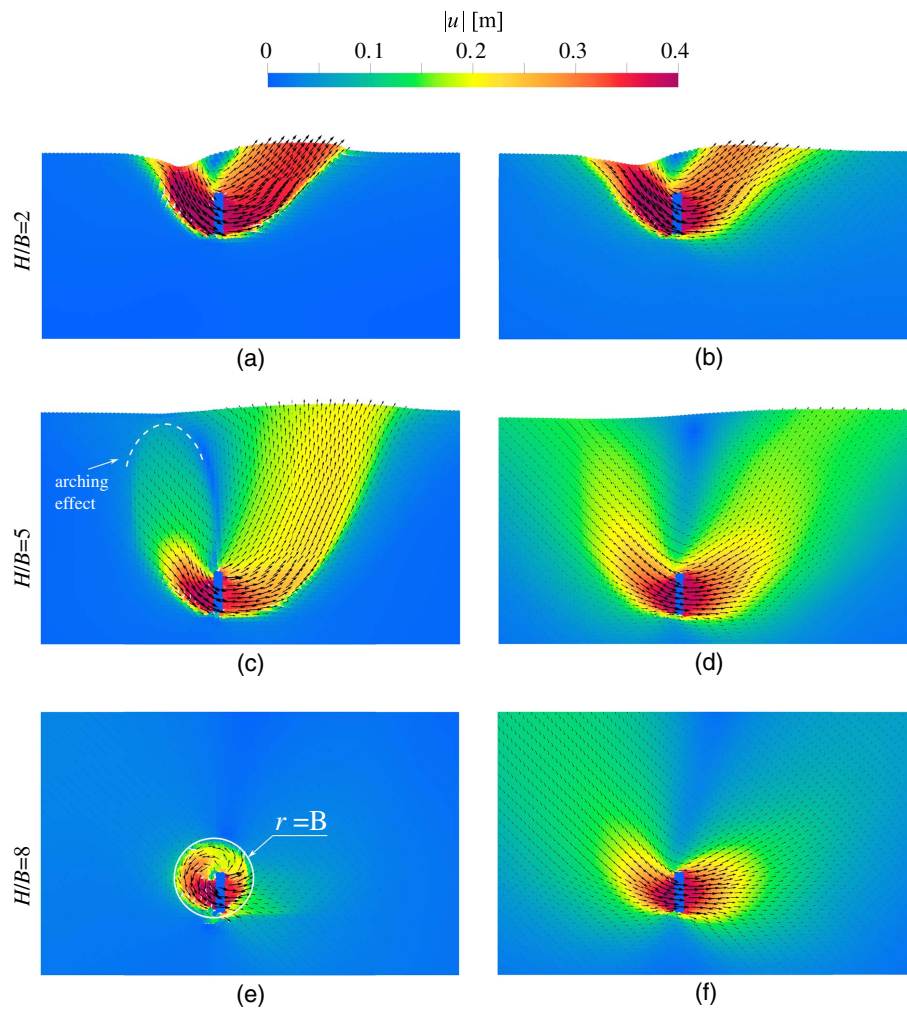


Fig. 10. Displacement contour for pullout of vertically placed plate anchor in sand at $d = 0.4B$: (a), (c), and (e), dense sand; and (b), (d), and (f), loose sand.

The increase in embedment depth causes appreciable differences in deformation patterns for the two sands. Take the case of $H/B = 5$, as an example. The movement of the anchor in the dense sand mobilizes a larger passive zone in the soil ahead than occurs in the loose sand case. The soil in the passive zone is pushed forward and upward along a slip surface with a nearly uniform velocity field before reaching the ground to form a heave. However, the extent of this behavior along the active side of the anchor in dense sand appears to be smaller than in loose sand. Interestingly, an arch-like structure appears to form close to the ground surface on the active side [Fig. 10(c)], displaying an interesting arching effect widely observed in granular media (Pardo and Sáez 2014). As the anchor moves, the soil behind the anchor collapses and fills the formed gap. However, the soil above the collapsing mass [see the dash line in Fig. 10(c)] remains intact, as its weight is transferred by the arch-like structure to the surrounding stationary soil. This arching effect may partially help to prevent excessive settlement of the ground surface, leading to a smaller mobilization zone on the active side than on the passive side. Similar observations were also reported by Rowe and Davis (1982) and Choudhary and Dash (2017). As for the loose sand case, the mobilized zones on both sides of the anchor appear to be largely similar due to the much smaller volumetric changes [Fig. 10(d)]. The displacement

field in the loose sand also appears to be continuous, without identifiable slip surfaces.

When the burial depth is further increased (e.g., $H/B = 8$), more localized deformation patterns emerge in the soil. As shown in Fig. 10(e), a local rotational mechanism dominates the deformation pattern for the deep vertically placed plate anchor in dense sand, due to the excessive vertical constraints imposed by the overlying soil. The soil in front of the anchor is pushed and rotates to flow around the top of the anchor, filling the gap left behind the anchor, similar to the deep horizontal anchor described above. The flow region can be approximately delineated by a circle with a radius of B centered at the upper edge of the anchor. Such local rotational mechanisms have also been reported by Biarez et al. (1965) and Choudhary and Dash (2017). Along with this flow-around phenomenon is the forward motion of the small part of the soil at the front toe of the anchor, albeit it is not apparent compared to the circle. In the case of loose sand, the deformation pattern is similar to that in the intermediate embedment depth [e.g., Fig. 10(d)]. However, it was found that the motion of soil in front of the anchor does not present as clear a preference for moving upward as that presented in Fig. 10(d), such that the displacement field hardly reaches the ground surface. The ground surface appears to fall more from the active zone behind the moving anchor in the loose sand case.

Failure Patterns

Typical failure mechanisms for vertically placed plate anchor in sand, indicated through the contour of equivalent von Mises strain ε_{eq} and rotation angle θ , are shown in Fig. 11. Although it is found that the major shear band invariably passes through the lower edge of the anchor, the failure pattern is significantly affected by the embedment ratio of the anchor as well as the soil conditions.

With dense sand, a general shear failure takes place over the range from shallow to intermediate embedment depths. After originating at the lower edge of the anchor, the shear band propagates horizontally by a small distance, then curves upward and finally reaches the ground surface. This shear band is the slip surface for the soil mass, which distinguishes the mobilization area from the intact soil [Figs. 10(a and c)]. A second shear band extends from the top of the anchor, propagates vertically, and further divides the mobilized region into two parts: the active zone and the passive zone. As the embedment depth increases, a local shear failure takes place [Fig. 11(e)]. Similarly, the major shear band originates from the same position and then curves upward. However, the overlying soil is so thick that it cannot reach the ground surface. Instead, it propagates by curving and eventually connects with the other end of the shear band, forming an approximate circle with its center close to the upper edge of the anchor. As for the shallow anchor in loose sand, the shear band at the active side extends to the ground surface. However, the shear band at the passive side is too blurred to be distinguished. This is consistent with the observation in its displacement field [Fig. 10(b)], wherein the change of the displacement is relatively smooth at the passive zone. In contrast to dense sand, for loose sand the transition from general shear failure to local shear failure occurs at a shallower embedment depth. For example, when the embedment ratio increases to $H/B = 5$, the shear failure is constrained locally. Two shear bands originate from the edge of the

anchor due to the sliding movement. Because of the higher pressure at the bottom of the anchor (Choudhary and Dash 2017), the lower shear band is longer in length and greater in intensity. Due to the relatively low strength and high porosity of the loose sand, none of those shear bands could reach the ground surface.

It is also of interest to investigate the rigid rotations in the soil sample, which are shown in Figs. 11(g–l). Albeit with different soil conditions and embedment ratios, the soil inside the major shear band, which passes through the bottom of the anchor, possesses a clockwise rotation angle in all cases, while the soil in the mobilization region, which is surrounded by the major shear band, more or less possesses a counterclockwise rotation angle. These rotation patterns reveal the underlying similarity between the general shear failure and the local failure, and somehow explain why the formula proposed by Biarez et al. (1965) could offer satisfying prediction of bearing capacity over a wide range of embedment ratios. Note that the rotation in some particular regions is almost imperceptible, including the triangular wedge ahead of the anchor and the major soil block in the passive zone. This is because the soil mass at these regions is displaced in a relatively uniform velocity and thus the shearing tendency is slight.

Cross-Scale Analyses of Underpinning Failure Mechanisms

The hierarchical coupling structure of the multiscale approach enables us to directly identify and link the dominant underpinning failure mechanisms at grain scales to interesting macroscopic phenomena. In this section, two material points were selected from the shallow horizontal plate anchor cases for cross-scale analyses. Point A was initially in a dense state (porosity $n \approx 0.157$) whereas Point B was in a loose state ($n \approx 0.198$). Both points are located

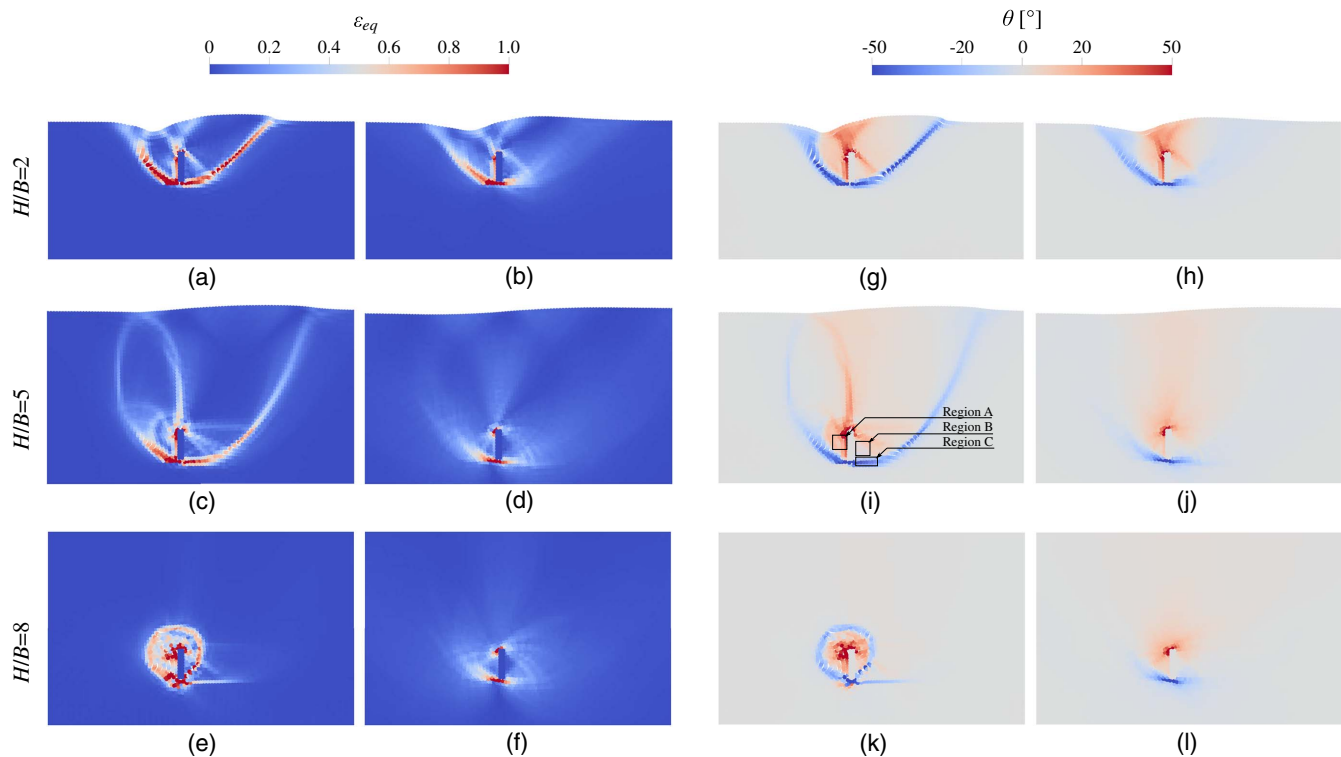


Fig. 11. Equivalent von Mises strain and rotation angle contour for vertically placed plate anchors in sand at $d = 0.4B$: (a), (c), (e), (g), (i), and (k), dense sand; and (b), (d), (f), (h), (j), and (l), loose sand.

inside the later-formed shear band, with positions marked in Figs. 9(a and b).

The evolutions of the deviatoric stress σ_q , stress ratio σ_q/σ_p , fabric anisotropy F_a , and porosity n for both chosen points during the entire uplift process are presented in Fig. 12. All these quantities were extracted from the homogenization of the corresponding RVEs during the simulated pullout process. Evidently, the movement of the anchor in the dense sand causes continuous shear, resulting in typical dense sand shear responses, as shown by Point A. Its deviatoric stress quickly increases to a peak of $\sigma_q \approx 15$ kPa shortly after the commencement of the uplift movement. Subsequently, it shows an obvious softening regime before reaching a plateau when $d/B > 0.2$. Other quantities, such as stress ratio σ_q/σ_p and fabric anisotropy F_a , also depict similar trends and stabilize at $\sigma_q/\sigma_p \approx 0.36$ and $F_a \approx 0.32$. During the entire movement, Point A undergoes a rather steady, extensive volumetric dilation, indicated by the increase of porosity n from 0.159 to 0.206. Point B, however, which was loaded from an initially loose state, does not show an appreciable peak deviatoric stress.

It is instructive to further discuss the above local responses based on critical state theory (CST) (Roscoe et al. 1958; Schofield and Wroth 1968; Zhao and Guo 2013). DEM studies (Yimsiri and Soga 2010; Zhao and Guo 2013) show that a granular soil, if sheared sufficiently, may reach a unique critical state with a steady stress ratio σ_q/σ_p , porosity n and fabric anisotropy F_a . Indeed, in the multiscale simulation, the selected material points appear to have reached a rather close critical state under sustained shear imposed by

the anchor pullout, as evidenced by the evolution curves shown in Fig. 12, where the state quantities for both points finally stabilize roughly at $\sigma_q = 7.05$ kPa, $\sigma_q/\sigma_p = 0.36$, $F_a = 0.32$, and $n = 0.206$, albeit with moderate fluctuations. After this state, the soil sample may evolve with a stable internal structure to resist the external load.

The above mesoscale analyses can be further correlated to the global response for better interpretation of the macroscopic observations, such as the displacement-load relation in Fig. 3. When the anchor is mobilized to a large displacement, the sand inside the generated shear band sustains substantial shear and reaches a critical state. For a shallowly embedded anchor, it is reasonable to expect that this resistance will eventually converge, as the resisting sand usually collapses in similar wedge-shaped patterns. For a deeply buried anchor, this may not necessarily hold since the influencing region of the localized failure is highly correlated to the characteristic of the resisting soil.

Cross-Scale Analyses of Soil-Anchor Interactions

The current MPM-DEM multiscale approach also manifests its capability in analyzing the highly nonlinear and complex local response of soil close to the anchor, which serves as a crucial step toward understanding the interaction of soil and structure. We take the vertically placed plate anchor embedded at the intermediate burial depth ($H/B = 5$) in dense sand as an example. As shown above, this case presents relatively more complex failure patterns

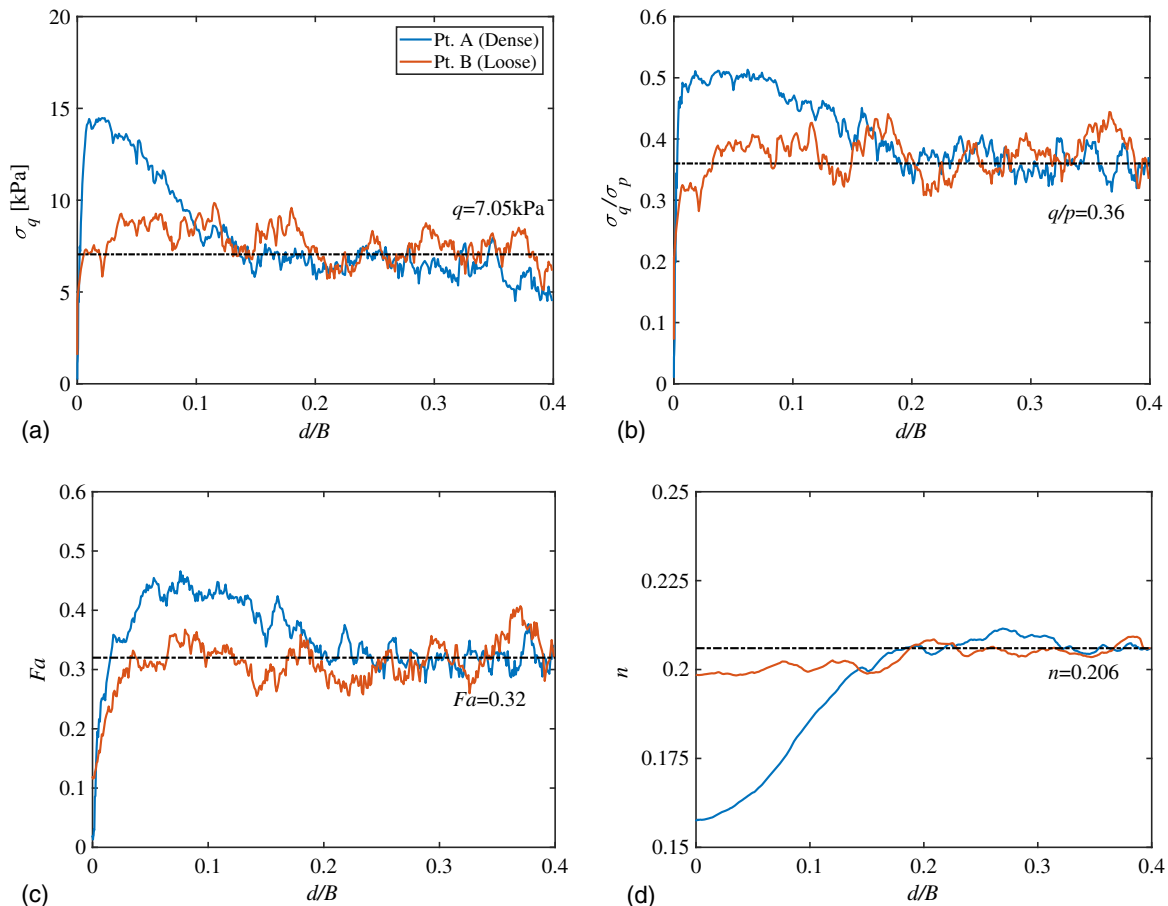


Fig. 12. Evolution curve for selected material points: (a) Deviatoric stress σ_q ; (b) stress ratio σ_q/σ_p ; (c) fabric anisotropy F_a ; and (d) porosity n . The locations of selected points are marked in Fig. 9.

than the others. As the soil adjacent to the anchor continuously collapses, rearranges and reaches equilibrium, the local response provoked by a single material point may prove to be highly fluctuating and unreliable. To better represent the local responses close to the anchor, three regions, namely, Regions A, B, and C, were chosen, wherein the homogenized responses from the windows were analyzed. As indicated in Fig. 11(i), Regions A and B are immediately adjacent to the anchor, located at the back and front side of the anchor, respectively. Region C is located inside the main slip line close to the lower edge of the anchor. Each of the three regions was chosen to contain around 15 material points, and their averaged state variables are discussed as follows.

Region A and Region B

The local material responses of Regions A and B, including deviatoric strain ε_q , porosity n , fabric anisotropy F_a , deviatoric stress σ_q , and lateral earth pressure coefficient K , are examined in Fig. 13. Both mean and range of the variables are presented. Clearly, the shear strain increases for both regions with the pullout of the anchor [Fig. 13(a)], but at a much faster rate in Region A than in B. At the final stage, the average for Region A ($\varepsilon_q = 0.55$) is roughly three times that for Region B ($\varepsilon_q = 0.18$). However, the two regions experience rather diverging volumetric changes: while Region A shows steady dilation (with porosity increasing from an initial $n = 0.158$ to a final $n = 0.198$), Region B undergoes contraction until a rather late stage of the pullout process [Fig. 13(b)]. The dilative response in Region A apparently accounts for its filling the gap caused by the lateral anchor movement and eventually results in a smaller mobilization area behind the anchor [Fig. 10(c)]. Indeed, Regions A and B experience active and passive failure, respectively. Their peak lateral earth pressure coefficient, determined from the RVE responses, as shown in Fig. 13(e), are $K \approx 0.5$

and $K \approx 2$, respectively. This differs from their respective theoretical values ($\tan^2(\pi/4 - \varphi'/2) = 0.33$ for K_a and $\tan^2(\pi/4 + \varphi'/2) = 3.02$ for K_p) according to Rankin's earth pressure theory, likely due to the complex geometry and mechanical interactions between the anchor and the soil.

Fabric anisotropy, derived directly from the particle-scale contact force network, has been widely used to characterize the microstructure of granular media (Guo and Zhao 2013). It is employed here to examine the microstructural changes in all three chosen regions. Intriguingly, it is found that, for all three regions, the rapid increase in F_a coincides exactly with the point where dilation and strength reduction occur. A similar characteristic was observed by Yimsiri and Soga (2010), based on their DEM analysis. For Region A, once the anchor movement is initiated, the horizontal confinement is reduced almost instantly with an approximately constant vertical overburden pressure. Release of the horizontal contact for RVEs inside Region A results in an increase in fabric anisotropy F_a to 0.45, while the deviatoric stress reaches a peak value of $\sigma_q \approx 18$ kPa. The peak of σ_q in Region A appears to occur slightly earlier than that of F_a , indicating there may be a delayed response in the soil adjusting to the permanent deformation, to reestablish proper fabric structure for resisting the applied stress change. As the movement continues, the soil behind the anchor slides down to fill the gap. The deviatoric stress in Region A decreases from its peak and stabilizes at a rather low level (e.g., $\sigma_q \approx 7$ kPa). The fabric anisotropy also undergoes a similar decreasing trend. Region B shows a rather different response. Its initial fabric is preserved while the deviatoric stress σ_q increases monotonically until $d/B = 0.14$. After $d/B = 0.14$, the initially formed fabric in Region B is altered, accompanied by a softening of the deviatoric stress from its peak $\sigma_q \approx 140$ kPa. Meanwhile, the fabric anisotropy shows an increase followed by a roughly stable value of around 0.26.

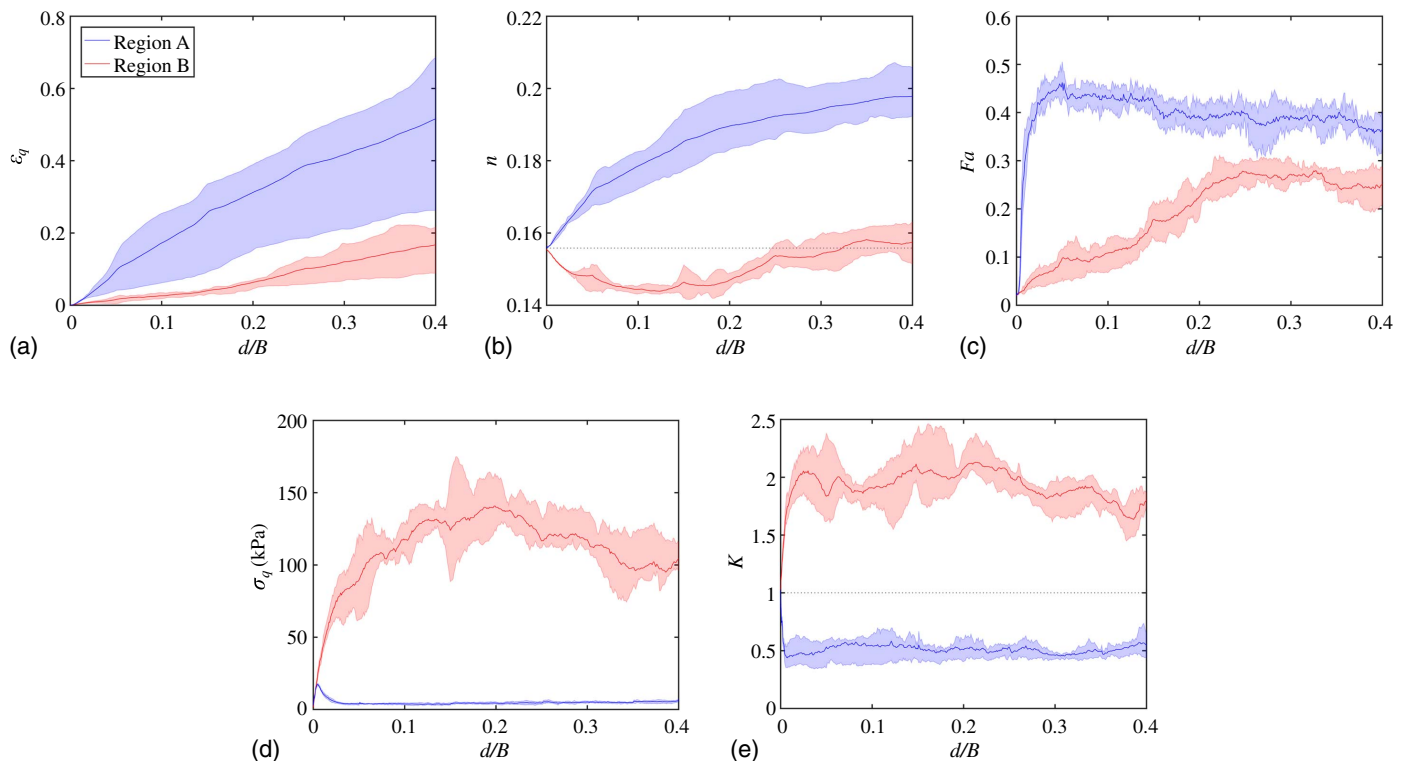


Fig. 13. Local material responses in Regions A and B: (a) deviatoric strain ε_q ; (b) porosity n ; (c) fabric anisotropy F_a ; (d) deviatoric stress σ_q ; and (e) lateral earth pressure K versus pullout displacement d/B . Shadows show the range of variables while solid lines show mean values.

Region C

Fig. 14 shows the local responses for Region C. As it is located inside the shear band close to the lower edge of the anchor, Region C experiences an intensive shearing, which is evidenced by the evolution curve [Fig. 14(a)], wherein the deviatoric strain rises up to $\varepsilon_q = 300\%$. Volumetric contraction is observed at the early stage of the anchor movement (e.g., $d/B < 0.02$), akin to that of Region B (which also rests at the same side of the anchor). However the soil in Region C quickly switches to dilation due to the intensive shearing. Above $d/B = 0.22$, the porosity reaches an ultimately stable value of $n = 0.191$. Despite the significant difference in loading history among Regions A, B, and C, the rapid boost of fabric anisotropy for Region C also takes place when the porosity is smallest, just before dilation (e.g., $d/B = 0.03$), suggesting a common trend in the development of microstructures at the commencement of the dilation. This observation confirms previous results reported by Yimsiri and Soga (2010). Fig. 14(d) shows that the deviatoric stress reaches its peak $\sigma_q = 85$ kPa at $d/B = 0.1$, followed by a continuous decrease due to strain softening. The intensive shearing also induces significant rotations for the material points in Region C, as depicted in Fig. 14(e), with a cumulative counterclockwise rotation up to 40° over the pulling process.

Stress Path and Force Chain

The stress paths shown in Fig. 15 further reveal the distinct loading history each region has undergone. As is seen from Fig. 15(a), the mean stress σ_p for Region A decreases monotonically, whereas its deviatoric stress σ_q undergoes an initial increase before dropping. As the stress path evolves toward the origin, a minimum strength is developed. In contrast, Region B maintains a relatively high stress state during the entire pullout process. At an early stage, the stress path in Region B is almost linear, with a slope of curve less than 1,

indicating that Region B is subjected to intensive compression from its surrounding soil. After $\sigma_p \approx 340$ kPa, its stress path reverses and shows apparent fluctuations. The steep stress path for Region C confirms that severe shearing occurs in this region. Although the final stress states for the three regions lie close to the critical state line (CSL, which can be obtained by shearing RVEs in pure DEM up to a large strain level), it does not imply that all regions reach critical state. As seen from the stress path in $\sigma_p - e$ space shown in Fig. 15(b), Region C fits closely to the CSL fitting curve when it develops maturely, but Region B is still far from CSL. Interestingly, the stress path of Region A shows it approaches a steady state flow failure, as envisioned by Verdugo and Ishihara (1996), when its active state continues to develop with the anchor moving further away from the region.

In addition to the stress path, it is also instructive to explore the microstructural changes of typical RVEs inside the aforementioned local regions during the pullout. Fig. 16 presents the force chain networks and the polar histograms of contact direction for three typical RVEs selected from the three regions. Fig. 16(a) indicates the RVE packing situated in Region A suffers from mild stretch and moderate rotation. Due to weak confinement in this active state in Region A, the force chains are only moderately stressed, with relatively thin force changes. The contacts show a preferential vertical alignment, as seen from the rose diagram, due to the overburden pressure being the principal stress in this zone. Comparatively, the RVE packing selected from Region B shows significantly smaller deformation with nearly rigid compression along the direction of anchor movement, but the horizontally orientated (tilting 15° or so upwards, as shown in the rose diagram) force chains are considerably stronger, clearly indicating the highly compressive stress state in this passive zone.

A more representative microstructural change of the large deformation nature of the anchor pullout problem is manifested in

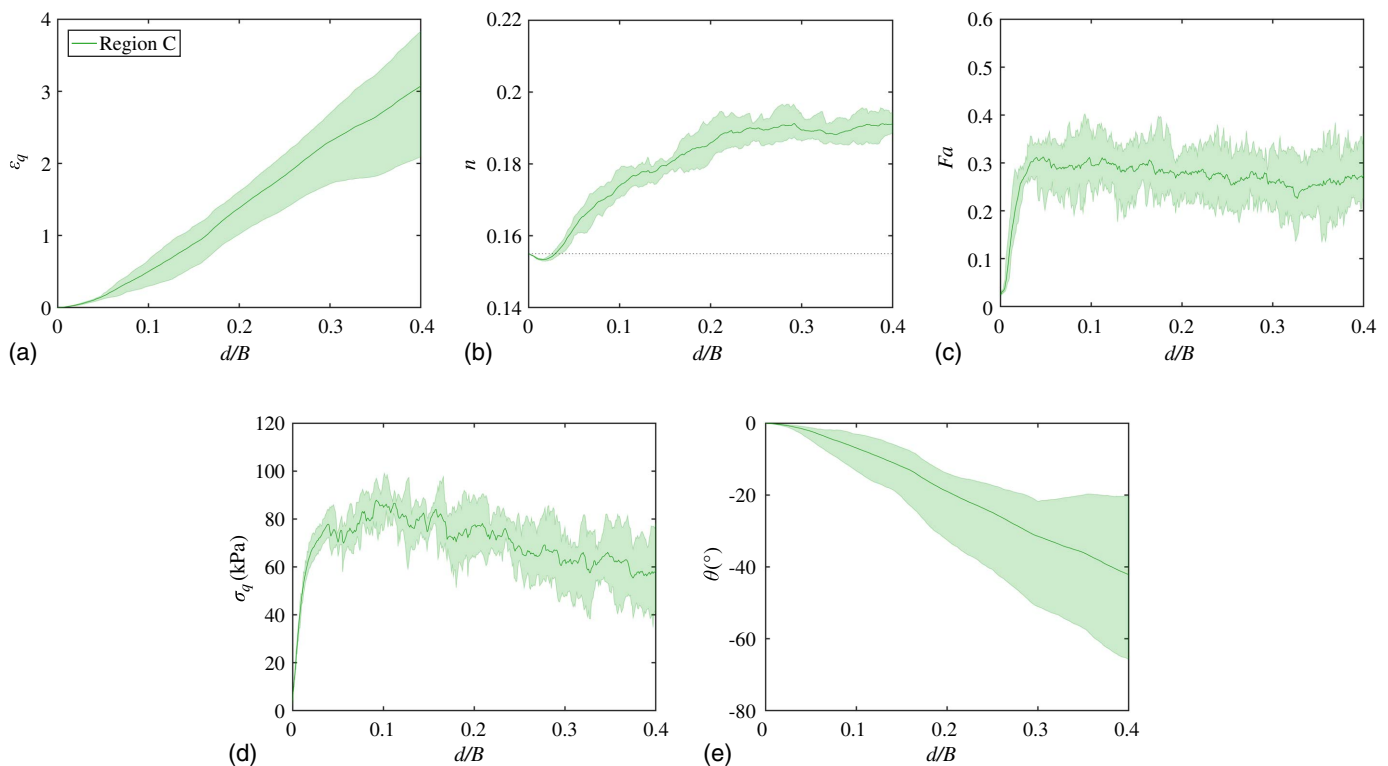


Fig. 14. Local responses for Region C: (a) deviatoric strain ε_q ; (b) porosity n ; (c) fabric anisotropy F_a ; (d) deviatoric stress σ_q ; and (e) rigid rotation angle θ . Shadows show the range of variables while solid lines show mean values.

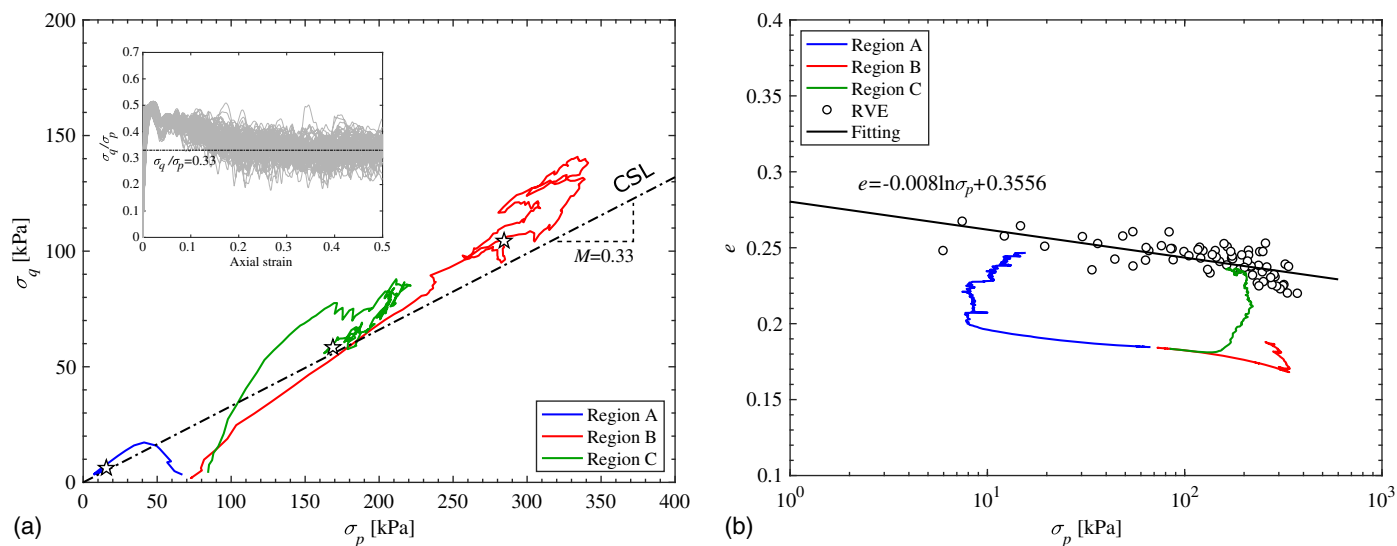


Fig. 15. Stress path in (a) $\sigma_p - \sigma_q$ space; and (b) $\sigma_p - e$ space for selected regions. The pentagram indicates the final stress state and the insertion shows the result of biaxial compression test in pure DEM simulation.

Fig. 16(c) for the RVE packing selected from Region C. The RVE within the major slip surface undergoes such a severe shear deformation that the entire packing becomes stretched and is accompanied by considerable rotation (its initial configuration is marked by red dotted square). Although the force network is considerably weaker than that in Region B, it remains continuous with a preferential orientation of 45° to the horizontal. The soil in this sliding zone clearly contributes to the bearing resistance to the anchor, although its effect is less significant than that in the passive zone. These observations about the microstructures of RVEs are consistent with the local responses shown in Figs. 13 and 14.

Conclusions

The pullout of either a horizontally or vertically placed plate anchor from granular sand has been computationally investigated by an innovative multiscale approach based on the hierarchical coupling of MPM and DEM. The multiscale approach invokes MPM to tackle large deformation simulation on the anchor pullout and adopts DEM to capture the complex material responses during large deformation on the mesoscale. The framework helps to bypass assumptions of phenomenological constitutive models in reproducing material responses for the challenging simulation, avoids complicated large deformation formulations of numerical schemes, and offers direct links between interesting macroscopic phenomena and their underlying physical mechanisms on the granular scale. The study emphasizes an alternative, future-looking pathway for engineers to analyse the bearing capacity of anchor bearing soils, and the associated deformation patterns and failure mechanisms. The key findings from this study are summarized as follows:

- The bearing capacity of supporting soil for a plate anchor is found to increase with the embedment depth, for both horizontally and vertically placed anchors. However, when the burial depth is deep enough, the increase in the breakout factor becomes less significant or even uncorrelated with the embedment depth, particularly for vertically placed plate anchors. Among available results in the literature, our multiscale predictions are consistent with those reported by Meyerhof and Adams (1968) and Biarez et al. (1965) for a horizontally placed plate anchor and vertically placed anchor, respectively.

- For a horizontally placed plate anchor, a truncated cone shape mobilization zone with a ground heave is found in dense sand for shallow to intermediate embedment depth cases. The failure is featured by a major shear band originating from the edge of the anchor and penetrating to the ground surface. Similar deformation patterns are also observed for shallow anchors in loose sand. The deformation patterns tend to be localized when the embedment depth of the anchor is deeper, i.e., the soil above the anchor flows around the edge of the anchor to fill the gap underneath, and shear failure occurs close to the edge of the anchor.
- For a vertically placed plate anchor, general shear failure takes place in both dense and loose sands when the embedment depth is shallow, wherein the soil is mobilized along a slip surface under the combined influence of anchor movement and gravity. When the embedment depth increases to an intermediate level, general shear failure patterns can still be observed in dense sand, where the mobilized active zone is much smaller than the passive zone due to significant differences in shear dilation. For the loose sand case, only two short shear bands are found close to the edge of the anchor, indicating a local shear failure mode. For deep anchors in dense sand, a local rotational failure becomes dominated, where the soil adjacent to the anchor rotates around the upper edge of the anchor as a cylindrical zone.

The current study offers a new perspective to existing experimental and numerical results on the pullout of anchors in sand. The cross-scale analyses provide new insights into the failure mechanisms of soil during anchor pullout, assisting engineers in evaluating the bearing capacity in anchor design. Nevertheless, there are two aspects that deserve further improvement: First, in the present study, the granular sand was modeled by assemblies of 2D disks in the DEM, which inevitably leads to unrealistic effective quantities, such as porosity, peak/residual homogenized stress, and dilation level (Mitchell and Soga 2005). Further studies should consider sand consisting of 3D irregularly shaped grains, to generate samples with more realistic particulate physics and overall strength characteristics, such as friction angle (Mollon and Zhao 2013; Kawamoto et al. 2018; Zhao and Zhao 2019). Second, the presented study considered plate anchor pullout in homogeneous soils under plane strain and drained conditions. Other factors, including anchor shapes in full 3D conditions, inhomogeneous soil profiles, and soil-water interactions, can be incorporated to render more realistic predictions.

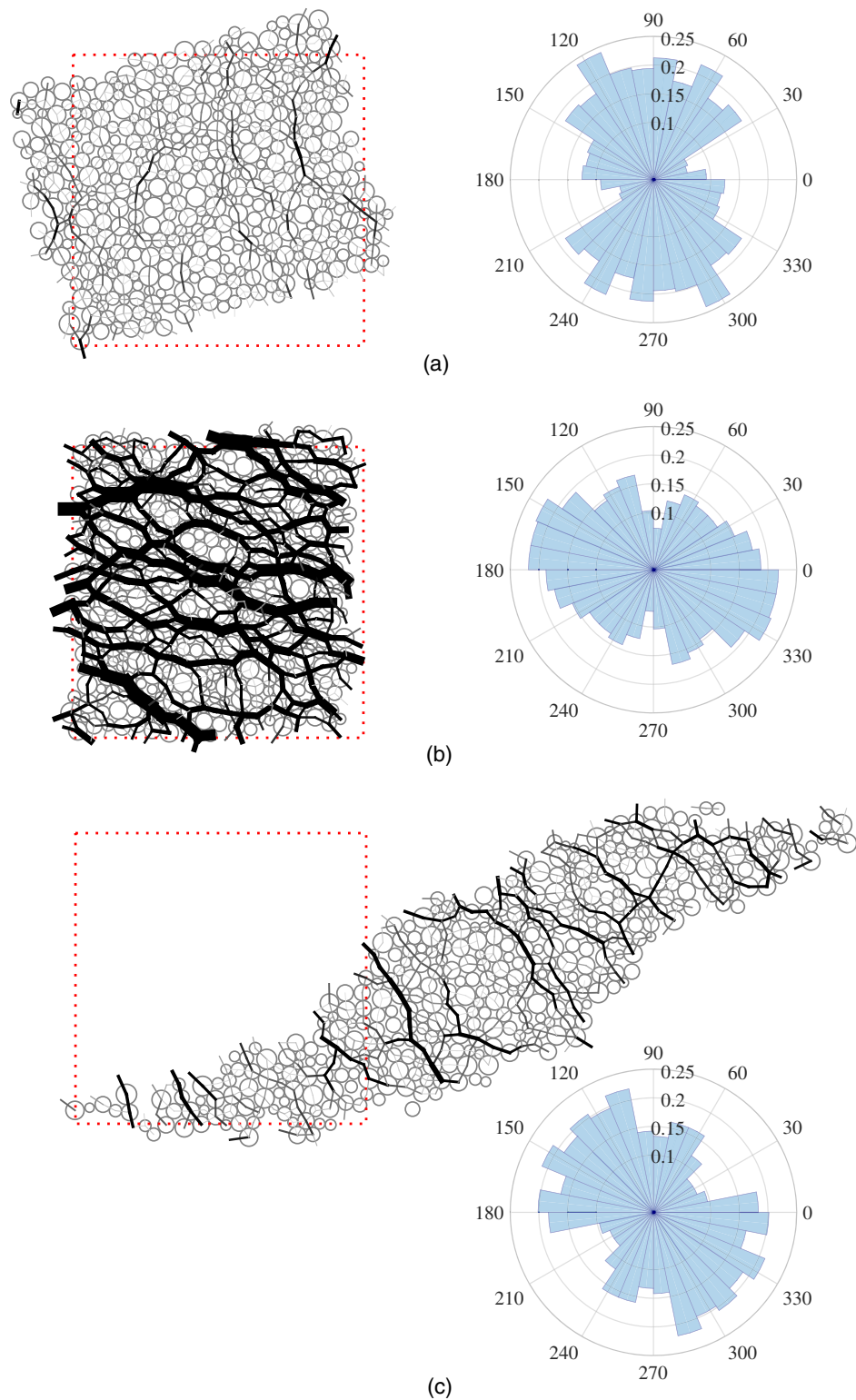


Fig. 16. Force chain network and polar histogram of contact direction for typical RVE in selected regions: (a) Region A; (b) Region B; and (c) Region C. Dash lines show initial configuration of RVE.

Appendix. Mesh Dependency

Similar to other mesh-based continuum approaches, the adopted MPM-DEM approach may suffer from the well-known mesh dependency issue. To evaluate the influence of mesh density on our simulations, the pullout of a horizontally placed anchor from dense sand with $H/B = 3$ was simulated with a finer mesh whose

element size is 0.05 m. The size of a material point was also set to 0.05 m to maintain the same PPC (particle-per-cell) number. The simulated displacement contours and load-displacement curves are shown in Fig. 17. It is clear that the simulations using different meshes yield rather similar deformation patterns and consistent anchor resistances. The case with a finer mesh (and smaller particle size) shows a slightly lower post-peak resistance, which is consistent

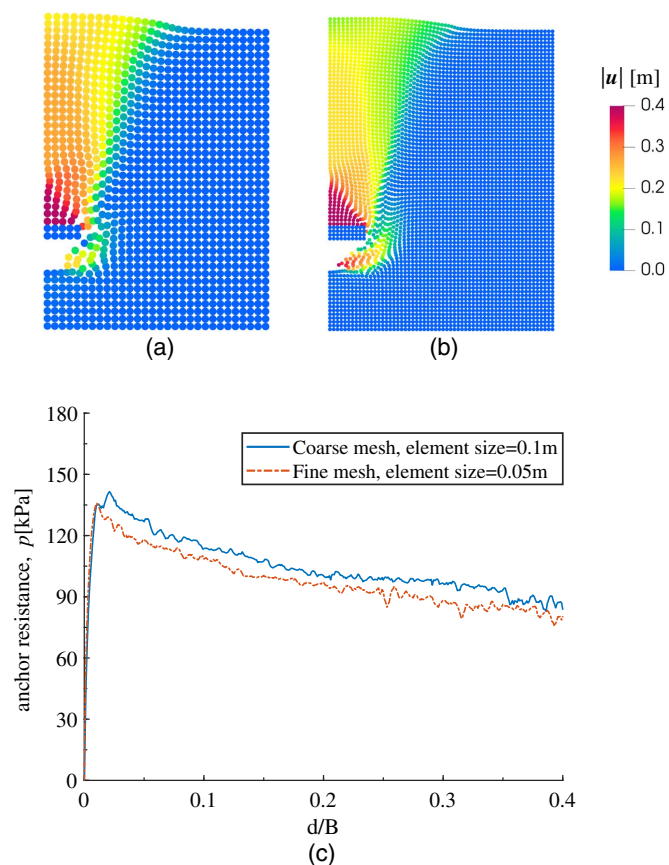


Fig. 17. Mesh sensitivity analyses for MPM-DEM multiscale approach: (a) displacement contour using coarse mesh with element size of 0.1 m; (b) displacement contour using fine mesh with element size of 0.05 m; and (c) load displacement responses for pullout of horizontally placed anchor from dense sand, $H/B = 3$.

with Liang and Zhao (2019). It is noteworthy that reducing the element size by half may cause an approximately eight times increase in computational costs, simply due to the remarkable increase in material point numbers (4 times) and computation steps (2 times). Therefore, we have chosen a relatively coarse mesh for the simulations in this study.

Data Availability Statement

All data, models, and code generated and used during this study are available from the corresponding author by request.

Acknowledgments

This study was financially supported by the National Natural Science Foundation of China (by Project No. 51679207), and the Research Grants Council of Hong Kong (by GRF Projects No. 16210017 and 16207319, TBRs Project No. T22-603/15N, and CRF Project No. C6012-15G).

References

Balla, A. 1961. "The resistance to breaking-out of mushroom foundations for pylons." In *Proc., 5th. Int. Conf. on Soil Mechanics and Foundation Engineering*, 569–576. Seattle: Allen Institute for AI.

- Bardenhagen, S. G., and E. M. Kober. 2004. "The generalized interpolation material point method." *Comp. Model. Eng. Sci.* 5 (6): 477–496.
- Biares, J., L.-M. Boucraut, and R. Negre. 1965. "Limiting equilibrium of vertical barriers subjected to translation and rotation forces." In Vol. 2 of *Proc., 6th Int. Conf. on Soil Mechanics and Foundation Engineering*, 368–372. Hoboken, NJ: Wiley.
- Ceccato, F., A. Bisson, and S. Cola. 2020. "Large displacement numerical study of 3D plate anchors." *Eur. J. Environ. Civ. Eng.* 24 (4): 520–538. <https://doi.org/10.1080/19648189.2017.1408498>.
- Chen, Z., K. K. Tho, C. F. Leung, and Y. K. Chow. 2013. "Influence of overburden pressure and soil rigidity on uplift behavior of square plate anchor in uniform clay." *Comput. Geotech.* 52 (Jul): 71–81. <https://doi.org/10.1016/j.compgeo.2013.04.002>.
- Cheuk, C. Y., D. J. White, and M. D. Bolton. 2008. "Uplift mechanisms of pipes buried in sand." *J. Geotech. Geoenviron. Eng.* 134 (2): 154–163. [https://doi.org/10.1061/\(ASCE\)1090-0241\(2008\)134:2\(154\)](https://doi.org/10.1061/(ASCE)1090-0241(2008)134:2(154)).
- Choudhary, A. K., and S. K. Dash. 2017. "Load-carrying mechanism of vertical plate anchors in sand." *Int. J. Geomech.* 17 (5): 04016116. [https://doi.org/10.1061/\(ASCE\)GM.1943-5622.0000813](https://doi.org/10.1061/(ASCE)GM.1943-5622.0000813).
- Christoffersen, J., M. M. Mehrabadi, and S. Nemat-Nasser. 1981. "A micro-mechanical description of granular material behavior." *J. Appl. Mech.* 48 (2): 339–344. <https://doi.org/10.1115/1.3157619>.
- Coetzee, C. J., P. A. Vermeer, and A. H. Basson. 2005. "The modelling of anchors using the material point method." *Int. J. Numer. Anal. Methods Geomech.* 29 (9): 879–895. <https://doi.org/10.1002/nag.439>.
- Cui, L., C. O'Sullivan, and S. O'Neill. 2007. "An analysis of the triaxial apparatus using a mixed boundary three-dimensional discrete element model." *Géotechnique* 57 (10): 831–844. <https://doi.org/10.1680/geot.2007.57.10.831>.
- Das, B. M., and S. K. Shukla. 2013. *Earth anchors*. Plantation, FL: J. Ross Publishing.
- Dickin, E. A. 1988. "Uplift behavior of horizontal anchor plates in sand." *J. Geotech. Eng.* 114 (11): 1300–1317. [https://doi.org/10.1061/\(ASCE\)0733-9410\(1988\)114:11\(1300\)](https://doi.org/10.1061/(ASCE)0733-9410(1988)114:11(1300)).
- Dickin, E. A., and M. Laman. 2007. "Uplift response of strip anchors in cohesionless soil." *Adv. Eng. Software* 38 (8–9): 618–625. <https://doi.org/10.1016/j.advengsoft.2006.08.041>.
- Dickin, E. A., and C. F. Leung. 1985. "Evaluation of design methods for vertical anchor plates." *J. Geotech. Eng.* 111 (4): 500–520. [https://doi.org/10.1061/\(ASCE\)0733-9410\(1985\)111:4\(500\)](https://doi.org/10.1061/(ASCE)0733-9410(1985)111:4(500)).
- Guo, N., and J. Zhao. 2013. "The signature of shear-induced anisotropy in granular media." *Comput. Geotech.* 47 (Jan): 1–15. <https://doi.org/10.1016/j.compgeo.2012.07.002>.
- Han, C., D. Wang, C. Gaudin, C. D. O'Loughlin, and M. J. Cassidy. 2016. "Behaviour of vertically loaded plate anchors under sustained uplift." *Géotechnique* 66 (8): 681–693. <https://doi.org/10.1680/jgeot.15.P.232>.
- Hu, Y., and M. F. Randolph. 1998. "A practical numerical approach for large deformation problems in soil." *Int. J. Numer. Anal. Methods Geomech.* 22 (5): 327–350. [https://doi.org/10.1002/\(SICI\)1096-9853\(199805\)22:5<327::AID-NAG920>3.0.CO;2-X](https://doi.org/10.1002/(SICI)1096-9853(199805)22:5<327::AID-NAG920>3.0.CO;2-X).
- Ilamparuthi, K., E. A. Dickin, and K. Muthukrisnaiah. 2002. "Experimental investigation of the uplift behaviour of circular plate anchors embedded in sand." *Can. Geotech. J.* 39 (3): 648–664. <https://doi.org/10.1139/t02-005>.
- Kawamoto, R., E. Andò, G. Viggiani, and J. E. Andrade. 2018. "All you need is shape: Predicting shear banding in sand with LS-DEM." *J. Mech. Phys. Solids* 111 (Feb): 375–392. <https://doi.org/10.1016/j.jmps.2017.10.003>.
- Liang, W., and J. Zhao. 2017. "Multiscale modelling of large deformations in granular materials." In *Proc., 21st Annual Conf. of HKSTAM 2017 and the 13th Jiangsu-Hong Kong Forum on Mechanics and Its Application*, 50. Hong Kong: Hong Kong SAR.
- Liang, W., and J. Zhao. 2019. "Multiscale modeling of large deformation in geomechanics." *Int. J. Numer. Anal. Methods Geomech.* 43 (5): 1080–1114. <https://doi.org/10.1002/nag.2921>.
- Liu, J., H. Hu, and L. Yu. 2013. "Experimental study on the pull-out performance of strip plate anchors in sand." In *Proc., 23rd Int. Offshore and Polar Engineering Conf.* Mountain View, CA: International Society of Offshore and Polar Engineers.

- Liu, J., M. Liu, and Z. Zhu. 2012. "Sand deformation around an uplift plate anchor." *J. Geotech. Geoenviron. Eng.* 138 (6): 728–737. [https://doi.org/10.1061/\(ASCE\)GT.1943-5606.0000633](https://doi.org/10.1061/(ASCE)GT.1943-5606.0000633).
- Merifield, R. S., and S. W. Sloan. 2006. "The ultimate pullout capacity of anchors in frictional soils." *Can. Geotech. J.* 43 (8): 852–868. <https://doi.org/10.1139/t06-052>.
- Meyerhof, G. G. 1973. "Uplift resistance of inclined anchors and piles." In Vol. 2 of *Proc., 8th ICSMFE*, 167–172. London: International Society for Soil Mechanics and Geotechnical Engineering.
- Meyerhof, G. G., and J. I. Adams. 1968. "The ultimate uplift capacity of foundations." *Can. Geotech. J.* 5 (4): 225–244. <https://doi.org/10.1139/t68-024>.
- Mindlin, R. D., and Deresiewicz, H. 1953. "Elastic spheres in contact under varying oblique forces." *J. Appl. Mech.* 20 (1): 327–344.
- Mitchell, J. K., and K. Soga. 2005. *Fundamentals of soil behavior*. New York: Wiley.
- Mollon, G., and J. Zhao. 2013. "Characterization of fluctuations in granular hopper flow." *Granular Matter* 15: 827–840. <https://doi.org/10.1007/s10035-013-0445-5>.
- Murray, E. J., and J. D. Geddes. 1987. "Uplift of anchor plates in sand." *J. Geotech. Eng.* 113 (3): 202–215. [https://doi.org/10.1061/\(ASCE\)0733-9410\(1987\)113:3\(202\)](https://doi.org/10.1061/(ASCE)0733-9410(1987)113:3(202)).
- Nairn, J. A. 2016. "Material point method (NairnMPM) and finite element analysis (NairnFEA) open-source software." Accessed April 25, 2021. http://osupdocs.forestry.oregonstate.edu/index.php/Main_Page.
- Nicot, F., N. Hadda, M. Guessasma, J. Fortin, and O. Millet. 2013. "On the definition of the stress tensor in granular media." *Int. J. Solids Struct.* 50 (14–15): 2508–2517. <https://doi.org/10.1016/j.ijsolstr.2013.04.001>.
- Oda, M. 1982. "Fabric tensor for discontinuous geological materials." *Soils Found.* 22 (4): 96–108. https://doi.org/10.3208/sandf1972.22.4_96.
- O'Sullivan, C., L. Cui, and S. C. O'Neill. 2008. "Discrete element analysis of the response of granular materials during cyclic loading." *Soils Found.* 48 (4): 511–530. <https://doi.org/10.3208/sandf.48.511>.
- Pardo, G., and E. Sáez. 2014. "Experimental and numerical study of arching soil effect in coarse sand." *Comput. Geotech.* 57 (Apr): 75–84. <https://doi.org/10.1016/j.compgeo.2014.01.005>.
- Randolph, M., and S. Gourvenec. 2017. *Offshore geotechnical engineering*. Boca Raton, FL: CRC Press.
- Roscoe, K. H., A. N. Schofield, and C. P. Wroth. 1958. "On the yielding of soils." *Géotechnique* 8 (1): 22–53. <https://doi.org/10.1680/geot.1958.8.1.22>.
- Rowe, R. K., and E. H. Davis. 1982. "The behaviour of anchor plates in sand." *Géotechnique* 32 (1): 25–41. <https://doi.org/10.1680/geot.1982.32.1.25>.
- Roy, K., B. Hawlader, S. Kenny, and I. Moore. 2016. "Finite element analysis of vertical strip anchors buried in dense sand subjected to lateral loading." In *Proc., 26th Int. Ocean and Polar Engineering Conf.* Mountain View, CA: International Society of Offshore and Polar Engineers.
- Roy, K., B. Hawlader, S. Kenny, and I. Moore. 2018a. "Lateral resistance of pipes and strip anchors buried in dense sand." *Can. Geotech. J.* 55 (12): 1812–1823. <https://doi.org/10.1139/cgj-2017-0492>.
- Roy, K., B. Hawlader, S. Kenny, and I. Moore. 2018b. "Upward pipe-soil interaction for shallowly buried pipelines in dense sand." *J. Geotech. Geoenviron. Eng.* 144 (11): 04018078. [https://doi.org/10.1061/\(ASCE\)GT.1943-5606.0001957](https://doi.org/10.1061/(ASCE)GT.1943-5606.0001957).
- Satake, M. 1982. "Fabric tensor in granular materials." In *Proc., IUTAM Conf. on Deformation and Flow of Granular Materials, 1982*, 63–68. Rotterdam, Netherlands: A.A. Balkema.
- Schofield, A. N., and C. P. Wroth. 1968. *Critical state soil mechanics*. New York: McGraw-Hill.
- Smilauer, V., et al. 2015. *Yade documentation*. 2nd ed. Geneva: Zenodo. <https://doi.org/10.5281/zenodo.34073>.
- Smith, C. C. 2012. "Limit loads for a shallow anchor/trapdoor embedded in a non-associative Coulomb soil." *Géotechnique* 62 (7): 563–571. <https://doi.org/10.1680/geot.10.P.136>.
- Terzaghi, K. 1951. *Theoretical soil mechanics*. London: Chapman and Hall.
- Tian, Y., M. F. Randolph, and M. J. Cassidy. 2015. "Analytical solution for ultimate embedment depth and potential holding capacity of plate anchors." *Géotechnique* 65 (6): 517–530. <https://doi.org/10.1680/geot.14.P.228>.
- Verdugo, R., and K. Ishihara. 1996. "The Steady State of Sandy Soils." *Soils Found.* 36 (2): 81–91. https://doi.org/10.3208/sandf.36.2_81.
- Vesic, A. S. 1973. "Analysis of ultimate loads of shallow foundations." *J. Soil Mech. Found. Div.* 99 (1): 45–73. <https://doi.org/10.1061/JSEFAQ.0001846>.
- Vesic, A. S., and J. A. Jones. 1971. "Breakout resistance of objects embedded in ocean bottom." *J. Soil Mech. Found. Div.* 97 (9): 1183–1205.
- Wang, D., Y. Hu, and M. F. Randolph. 2010. "Three-dimensional large deformation finite-element analysis of plate anchors in uniform clay." *J. Geotech. Geoenviron. Eng.* 136 (2): 355–365. [https://doi.org/10.1061/\(ASCE\)GT.1943-5606.0000210](https://doi.org/10.1061/(ASCE)GT.1943-5606.0000210).
- Wei, J., D. Huang, and G. Wang. 2020. "Fabric evolution of granular soils under multidirectional cyclic loading." *Acta Geotech.* 15 (9): 2529–2543. <https://doi.org/10.1007/s11440-020-00942-8>.
- White, D. J., C. Y. Cheuk, and M. D. Bolton. 2008. "The uplift resistance of pipes and plate anchors buried in sand." *Géotechnique* 58 (10): 771–779. <https://doi.org/10.1680/geot.2008.3692>.
- Yang, Y., and H. S. Yu. 2010. "Finite element analysis of anchor plates using non-coaxial models." *J. Rock Mech. Geotech. Eng.* 2 (2): 178–187. <https://doi.org/10.3724/SP.J.1235.2010.00178>.
- Yimsiri, S., and K. Soga. 2000. "Micromechanics-based stress-strain behaviour of soils at small strains." *Géotechnique* 50 (5): 559–571. <https://doi.org/10.1680/geot.2000.50.5.559>.
- Yimsiri, S., and K. Soga. 2010. "DEM analysis of soil fabric effects on behaviour of sand." *Géotechnique* 60 (6): 483–495. <https://doi.org/10.1680/geot.2010.60.6.483>.
- Yimsiri, S., K. Soga, K. Yoshizaki, G. R. Dasari, and T. D. O'Rourke. 2004. "Lateral and upward soil-pipeline interactions in sand for deep embedment conditions." *J. Geotech. Geoenviron. Eng.* 130 (8): 830–842. [https://doi.org/10.1061/\(ASCE\)1090-0241\(2004\)130:8\(830\)](https://doi.org/10.1061/(ASCE)1090-0241(2004)130:8(830)).
- Yu, L., J. Liu, X. J. Kong, and Y. Hu. 2008. "Three-dimensional RITSS large displacement finite element method for penetration of foundations into soil." *Comput. Geotech.* 35 (3): 372–382. <https://doi.org/10.1016/j.compgeo.2007.08.007>.
- Zhao, J., and N. Guo. 2013. "Unique critical state characteristics in granular media considering fabric anisotropy." *Géotechnique* 63 (8): 695–704. <https://doi.org/10.1680/geot.12.P.040>.
- Zhao, J., and N. Guo. 2014. "Rotational resistance and shear-induced anisotropy in granular media." *Acta Mech. Solida Sin.* 27 (1): 1–14. [https://doi.org/10.1016/S0894-9166\(14\)60012-4](https://doi.org/10.1016/S0894-9166(14)60012-4).
- Zhao, S., T. M. Evans, and X. Zhou. 2018. "Effects of curvature-related DEM contact model on the macro- and micro-mechanical behaviours of granular soils." *Géotechnique* 68 (12): 1085–1098. <https://doi.org/10.1680/jgeot.17.P.158>.
- Zhao, S., and J. Zhao. 2019. "A poly-superellipsoid-based approach on particle morphology for DEM modeling of granular media." *Int. J. Numer. Anal. Methods Geomech.* 43 (13): 2147–2169. <https://doi.org/10.1002/nag.2951>.